Commun. Comput. Phys.
doi: 10.4208/cicp.OA-2025-0113

Vol. **40**, No. 1, pp. 88-128
July 2026

A Novel High-Resolution TENO Scheme with Adaptive Artificial Anti-Diffusion

Velmani Murugesan[1] and Manoj T. Nair[1,*]

[1] *Department of Aerospace Engineering, Indian Institute of Space Science and Technology, Thiruvananthapuram, 695 547, Kerala, India.*

Communicated by Chi-Wang Shu

Received 28 April 2025; Accepted (in revised version) 9 August 2025

Abstract. Low-dissipation higher-order approaches are crucial for flows characterized by shocks and turbulence. The broad applicability of conventional WENO/TENO systems for accurately capturing shocks makes them a preferred option for simulating complex flow phenomena. Nonetheless, the inherent numerical diffusion in these techniques poses a significant challenge in simulating multiscale turbulent flow. This study mitigates the inherent numerical damping by using locally adaptive higher-order artificial anti-diffusion. A switching function quantifies the extent of anti-dissipation in the smooth zone and assesses the local variation of flow field variables. To assure stability, the anti-diffusion coefficient is meticulously assessed using two fixed free parameters. Next strategy utilizes a fourth-order central difference scheme in the highly smooth region, incorporating an additional coefficient modified in a binary fashion. The adaptive regulating parameter C_T in the fifth-order TENO scheme is integrated with the anti-diffusive function. It is recognized that the new scheme exhibits less numerical diffusion than the original TENO scheme. This is also reflected in the numerical experiments, encompassing a series of benchmark test scenarios featuring shock and fine-scale structures. It is shown that the proposed scheme could resolve the turbulent scales with much higher resolution and capture the shock sharply. It is worth noting that these strategies can easily be implemented in the other variations of the TENO scheme.

AMS subject classifications: 35L65, 65M08, 76F05, 76L05, 76J20, 76N15

Key words: ENO-like stencil selection, adaptive artificial anti-diffusion, WENO, TENO, low-dissipation schemes, fourth-order central difference.

*Corresponding author. *Email addresses:* velmanim.21@res.iist.ac.in (V. Murugesan), manojtnair@iist.ac.in (M. T. Nair)

1 Introduction

The numerical simulation of discontinuities (e.g., shock waves), multiscale structures (e.g., turbulence) and their interactions poses a significant challenge in Computational Fluid Dynamics (CFD). Numerical models must have adequate dissipation to effectively capture the shock and contact waves to prevent Gibbs oscillations induced by dispersion. Conversely, resolving fine scales in a turbulent field necessitates minimal numerical dissipation. This demand disparity makes it difficult to design numerical schemes until shock-capturing schemes were developed. Initial shock capturing approaches, such as Godunov's scheme [1] and Total Variation Diminishing (TVD) schemes [2–5] can capture discontinuities in complex flow problems. Although these methods have been used in compressible flow simulation, they would smear the shock waves due to the high inherent numerical diffusion. Higher-order techniques, such as Essentially Non-Oscillatory (ENO) [6,7] and Weighed Essentially Non-Oscillatory (WENO) [8,9] address this issue. The ENO scheme reconstructs the flux at the cell interface using the smoothest stencil.

In contrast, the WENO method estimates the interface flux using a linear combination of all substencils based on their weighted contributions. The WENO approach ensures the highest accuracy in smooth areas, whereas at discontinuities, the ENO characteristics are obtained. Balsara and Shu [10] extend this scheme to a higher order. Nonetheless, the smooth zone has a strong intrinsic numerical diffusion, which damps the vortical scales. The WENO scheme suffers from accuracy deterioration at the critical point where the first derivative approaches zero, but the third derivative remains non-zero [11, 12]. The WENO-M [13], WENO-Z [14], and WENO-CU6 [15] schemes were developed to improve the WENO schemes. These approaches have the potential to significantly reduce numerical dissipation while recovering formal order accuracy at local extrema. Ha et al. [16] introduced the WENO-NS technique, which evaluates the smoothness indicator using the generalized undivided difference operator, resulting in improved order of accuracy. The WENO-P scheme addresses an issue with the WENO-NS system's unbalanced stencil contribution [17]. Xu and Shu [18] attempted to reduce the numerical dissipation of WENO schemes using the anti-diffusive correction previously applied to first-order systems.

Despite the numerical damping, the aforementioned WENO schemes have superior shock-capturing capabilities. The reason for this severe damping is that the schemes fail to converge to optimal weights in smooth regions. Fu et al. [19–21] presented the family of Targeted Essentially Non-Oscillatory (TENO) schemes of different orders to address this issue. The primary characteristics of the TENO strategy are the scale separation [22] and the ENO-like stencil selection, which aligns the nonlinear weights with the linear ones in highly smooth regions. This method is also equipped with a regulating parameter, which manipulates the spectral properties of the scheme and can either be kept constant or modified based on local criteria. The latter approach is successfully executed in the TENO-A scheme, wherein the parameter is adjusted according to the local smoothness [23]. Wibisono et al. [24] used a Hermite polynomial approximation in the TENO

approach to attain high resolution of small-scale structures. A detailed evaluation of the TENO system and its descendants is provided in [25]. Takagi et al. [26] developed the TENO-THINC hybrid system to enhance discontinuity resolution. This approach approximates the shock region using the tangent hyperbolic function rather than the polynomial function, resulting in a higher resolution for capturing discontinuities. Yang et al. [27] presented free parameters that eliminate the leading truncation error in the polynomial approximation, increasing the order of accuracy to sixth. This technique was applied to the TENO-THINC scheme, significantly improving overall resolution, particularly in the vortex structures near the strong discontinuities. Liang and Fu [28] have devised a non-polynomial Gaussian RBF-based reconstruction for resolving small scales in the smooth region and deployed the THINC reconstruction for discontinuity.

This paper proposes a locally adaptive anti-diffusive correction function within the fifth-order TENO5 scheme to enhance the overall scheme accuracy in the turbulence region and effectively resolve the multiscale structures. This new TENO Adaptive Anti-Diffusion (TENO5AAD) scheme integrates three adaptive techniques. First, the excessive in-built numerical dissipation of the TENO5 scheme is alleviated by the higher-order anti-diffusive term, which ensures better resolution in capturing turbulent scales. Second, a switching parameter enforces the scheme to the fourth-order central difference scheme in the highly smooth region, where the standard TENO5 scheme has linear weights. The anti-diffusion coefficient and the switching parameter are both determined through local smoothness, which is estimated by a switching function. The third strategy is adaptive C_T within the TENO5 framework, which is executed in the TENO5A scheme. However, we relaxed this variation through a new function due to the introduction of anti-diffusion and stability considerations. The set of challenging numerical benchmark test cases is conducted. The results reveal that the present scheme captures fine-scale vortical structures more effectively than the standard TENO5 scheme.

The remaining sections are organised as follows: Section 2 briefly summarises the TENO5 and TENO5A schemes. Section 3 describes the adaptive anti-diffusive strategies employed in the TENO5 scheme. Section 4 assesses the performance of the current method using numerical experiments with shock and multiscale structures.

2 Review of Targeted Essentially Non-Oscillatory (TENO) schemes

Considering the one-dimensional hyperbolic conservation law

$$\frac{\partial u}{\partial t}+\frac{\partial f(u)}{\partial x}=0. \tag{2.1}$$

The flux derivative is estimated in the conservative form as

$$\left(\frac{\partial f}{\partial x}\right)_{x_i}=\frac{\hat{f}_{i+1/2}-\hat{f}_{i-1/2}}{\Delta x}, \tag{2.2}$$

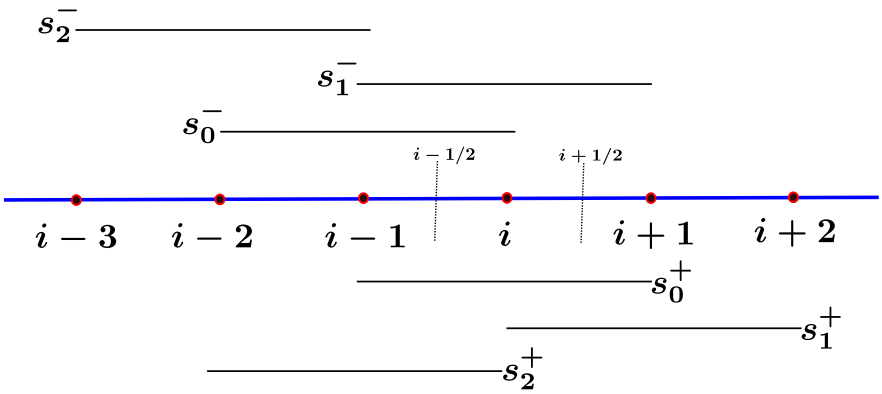

Figure 1: Schematic diagram of stencil arrangement in TENO scheme.

where $\hat{f}$ is the primitive function defined implicitly as

$$f(x)=\frac{1}{\Delta x}\int_{x_{i-1/2}}^{x_{i+1/2}}\hat{f}(\xi)\,d\xi. \tag{2.3}$$

2.1 Candidate stencils

Unlike the conventional fifth-order WENO scheme, the TENO scheme [19] is constructed by rearranging the stencil, as illustrated in Fig. 1. This arrangement is advantageous, particularly in a scenario characterised by multiple discontinuities. In the fifth-order approximation, the flux function of each candidate stencil S_0, S_1 and S_2 is approximated by a second-degree polynomial function, which is expressed as

$$\begin{aligned}
\hat{f}^{(0)}_{i+1/2}&=\frac{1}{6}(-f_{i-1}+5f_i+2f_{i+1}),\\
\hat{f}^{(1)}_{i+1/2}&=\frac{1}{6}(2f_i+5f_{i+1}-f_{i+2}),\\
\hat{f}^{(2)}_{i+1/2}&=\frac{1}{6}(2f_{i-2}-7f_{i-1}+11f_i).
\end{aligned} \tag{2.4}$$

The final reconstructed flux at the cell interface $x_{i+1/2}$ is estimated by

$$\hat{f}_{i+1/2}=\sum_{k=0}^{2}\omega_k\hat{f}^{(k)}_{i+1/2}. \tag{2.5}$$

The corresponding weight ω_k of each substencil is calculated based on the contribution and smoothness of the function of the particular substencil. The linear weights for the fifth-order approximation are $\bar{\omega}_0=0.6$, $\bar{\omega}_1=0.3$ and $\bar{\omega}_2=0.1$.

2.2 ENO-like stencil selection

The smoothness indicator [11] is defined as

$$\beta_k = \sum_{l=1}^{2} \Delta x^{2l-1} \int_{x_{i-1/2}}^{x_{i+1/2}} \left[\frac{d^l \hat{f}^{(k)}}{dx^l} \right]^2 dx. \tag{2.6}$$

The precise formulation for the smoothness indicator of each substencil is provided by

$$\begin{aligned}
\beta_0 &= \frac{13}{12}(f_{i-1}-2f_i+f_{i+1})^2+\frac{1}{4}(f_{i-1}-f_{i+1})^2,\\
\beta_1 &= \frac{13}{12}(f_i-2f_{i+1}+f_{i+2})^2+\frac{1}{4}(3f_i-4f_{i+1}+f_{i+2})^2,\\
\beta_2 &= \frac{13}{12}(f_{i-2}-2f_{i-1}+f_i)^2+\frac{1}{4}(f_{i-2}-4f_{i-1}+3f_i)^2.
\end{aligned} \tag{2.7}$$

By defining the global smoothness indicator, $\tau = |\beta_1 - \beta_2|$, the nonlinear weights are evaluated as

$$\gamma_k = \left(C + \frac{\tau}{\beta_k + \epsilon} \right)^q. \tag{2.8}$$

The integer power q is specified as a significant value, often $q = 6$, with $C = 1$. The parameter $\epsilon = 10^{-40}$ is employed to prevent division by zero. Eq. (2.8) utilises a robust scale separation approach between the smooth and discontinuous regions. Then, the weights γ_k are normalized as

$$\chi_k = \frac{\gamma_k}{\sum_{p=0}^{2} \gamma_p}. \tag{2.9}$$

The next step is to estimate the TENO weights based on the ENO-like stencil selection with a sharp cutoff function, which is defined as

$$\delta_k = \begin{cases} 0, & \text{if } \chi_k < C_T, \\ 1, & \text{otherwise.} \end{cases} \tag{2.10}$$

The parameter C_T acts as the barrier between the smooth and non-smooth regions in the wavenumber space. Eq. (2.10) selects the smooth stencil that asymptotically converges to the optimal weight and adapts in a binary way. The non-smooth stencil is excluded from the final reconstruction. The final TENO weights are given as

$$\omega_k = \frac{\bar{\omega}_k \delta_k}{\sum_{p=0}^{2} \bar{\omega}_p \delta_p}. \tag{2.11}$$

2.3 TENO5A scheme

In the standard TENO5 scheme, the regulating parameter C_T remains fixed (usually 10^{-5}) regardless of local smoothness. This scheme outperforms the WENO scheme in resolving the turbulence scales and capturing shocks sharply. However, it is possible to diminish the numerical diffusion in the highly smooth region by adjusting C_T in accordance with the local smoothness [23]. A discontinuity detector [29] used in this instance is

$$m = 1 - \min\left(1, \frac{\eta_{i+1/2}}{C_r}\right), \tag{2.12}$$

where

$$\eta_{i+1/2} = \min(\eta_{i-1}, \eta_i, \eta_{i+1}), \tag{2.13}$$

and

$$\eta_i = \frac{2ab+\zeta}{a^2+b^2+\zeta}, \tag{2.14}$$

$$\begin{aligned} &a = |f_i - f_{i-1}|, \quad b = |f_{i+1} - f_i|, \\ &\zeta = \frac{0.9C_r}{1-0.9C_r}\xi^2. \end{aligned} \tag{2.15}$$

The parameters are $\xi = 10^{-3}$ and $C_r = 0.24$. C_T is adjusted based on the value of m, which is defined as [23]

$$\begin{aligned} &g(m) = (1-m)^4(1+4m), \\ &\bar{\beta} = 10 - 5(1-g(m)), \\ &C_T = 10^{-\lfloor \bar{\beta} \rfloor}, \end{aligned} \tag{2.16}$$

in which $\lfloor\rfloor$ denotes the Gauss bracket, $g(m)$ represents the smooth mapping function. In the smooth region, the value of m approaches zero and C_T reduces to 10^{-10}. When $m \approx 1$, then C_T increases to 10^{-5}, which is suitable for shock capturing. This induces the dynamic adaptation of the value of C_T and nonlinear dissipation according to the local condition.

3 TENO scheme with adaptive artificial anti-diffusion

Consider the hyperbolic conservation law

$$\frac{\partial u}{\partial t} + \frac{\partial f}{\partial x} = 0. \tag{3.1}$$

Using the finite volume approach, Eq. (3.1) can be written in semi-discrete form as

$$\frac{du}{dt} + \frac{f_{i+1/2} - f_{i-1/2}}{\Delta x} = 0. \tag{3.2}$$

The interface flux is defined as $f_{i+1/2}=f(\hat{u}_{i+1/2})$. u and $\hat{u}$ can be related as

$$u(x)=\frac{1}{\Delta x}\int_{x_{i-1/2}}^{x_{i+1/2}}\hat{u}(x)dx. \tag{3.3}$$

For the fifth-order central-upwind biased scheme, the cell interface approximation would be

$$\hat{u}^C_{i+1/2}=\frac{1}{60}(2u_{i-2}-13u_{i-1}+47u_i+27u_{i+1}-3u_{i+2}). \tag{3.4}$$

Splitting Eq. (3.4) into fourth-order central difference and dissipation (hyper-viscous) terms as [12]

$$\hat{u}^C_{i+1/2}=\underbrace{\frac{-u_{i-1}+7u_i+7u_{i+1}-u_{i+2}}{12}}_{\text{central part}}+\underbrace{\frac{u_{i-2}-4u_{i-1}+6u_i-4u_{i+1}+u_{i+2}}{30}}_{\text{dissipation part}}. \tag{3.5}$$

Alternatively, the TENO reconstruction at the cell interface could be

$$\hat{u}_{i+1/2}=\sum_{k=0}^{2}\omega_k u^{(k)}_{i+1/2}. \tag{3.6}$$

The expression of $u^{(k)}_{i+1/2}$ of each candidate stencil is given in Eq. (2.4). It is well known that Eq. (3.6) converges to Eq. (3.5) in the smooth region. On replacing $\omega_0=1-\omega_1-\omega_2$ and using Eq. (3.6), we get

$$\begin{aligned}\hat{u}_{i+1/2}=&\frac{1}{12}(-u_{i-1}+7u_i+7u_{i+1}-u_{i+2})+\frac{1}{3}\omega_2(u_{i-2}-3u_{i-1}+3u_i-u_{i+1})\\&+\frac{1}{6}\left(\omega_1-\frac{1}{2}\right)(u_{i-1}-3u_i+3u_{i+1}-u_{i+2}).\end{aligned} \tag{3.7}$$

Now, let's define $\Delta u^{\pm}_{l+1/2}=u^{\pm}_{l+1}-u^{\pm}_l$. The reconstruction at the interface is split into left (+) and right (-) states as

$$\begin{aligned}\hat{u}^+_{i+1/2}=&\frac{1}{12}(-u^+_{i-1}+7u^+_i+7u^+_{i+1}-u^+_{i+2})\\&-\phi\left(\Delta u^+_{i-3/2},\Delta u^+_{i-1/2},\Delta u^+_{i+1/2},\Delta u^+_{i+3/2}\right),\\\hat{u}^-_{i+1/2}=&\frac{1}{12}(-u^-_{i-1}+7u^-_i+7u^-_{i+1}-u^-_{i+2})\\&+\phi\left(\Delta u^-_{i+5/2},\Delta u^-_{i+3/2},\Delta u^-_{i+1/2},\Delta u^-_{i-1/2}\right).\end{aligned} \tag{3.8}$$

The dissipation function ϕ is defined as

$$\phi(a,b,c,d)=\frac{1}{3}\omega_2(a-2b+c)+\frac{1}{6}\left(\omega_1-\frac{1}{2}\right)(b-2c+d). \tag{3.9}$$

Adding $\hat{u}^{+}_{i+1/2}$ and $\hat{u}^{-}_{i+1/2}$, we get the reconstruction at the interface as

$$\begin{aligned}\hat{u}_{i+1/2} = \frac{1}{12}(-u_{i-1}+7u_i+7u_{i+1}-u_{i+2}) \\ -\phi\left(\Delta u^{+}_{i-3/2},\Delta u^{+}_{i-1/2},\Delta u^{+}_{i+1/2},\Delta u^{+}_{i+3/2}\right) \\ +\phi\left(\Delta u^{-}_{i+5/2},\Delta u^{-}_{i+3/2},\Delta u^{-}_{i+1/2},\Delta u^{-}_{i-1/2}\right).\end{aligned} \tag{3.10}$$

3.1 Local adaptive artificial anti-diffusion

The artificial anti-diffusive flux is added in Eq. (3.1) as

$$\frac{\partial u}{\partial t}+\frac{\partial \widetilde{f}}{\partial x}=0, \tag{3.11}$$

$\widetilde{f}$ is the modified flux function that incorporates the anti-diffusive function. In this way, it is possible to preserve the overall scheme stability without much deviation. Analogous to the convective flux derivative (f), we can differentiate this modified flux derivative in its conservative form as

$$\frac{du}{dt}+\frac{\widetilde{f}_{i+1/2}-\widetilde{f}_{i-1/2}}{\Delta x}=0. \tag{3.12}$$

For anti-diffusion, we deploy the central difference formulation of the fourth derivative with an adaptive coefficient. The anti-diffusive function at the interface $u^{*}_{i+1/2}$ is articulated as

$$u^{*}_{i+1/2}=\lambda_{1,i+1/2}(-u_{i-1}+3u_i-3u_{i+1}+u_{i+2}). \tag{3.13}$$

$\lambda_{1,i+1/2}\geq 0$ is the local anti-diffusive coefficient at the interface $x_{i+1/2}$. To define $\lambda_{1,i+1/2}$, we utilize a switching function, that is given as

$$s_{\psi,i}=\left(\frac{\left|\Delta\psi_{i+1/2}-\Delta\psi_{i-1/2}\right|}{\left|\Delta\psi_{i+1/2}\right|+\left|\Delta\psi_{i-1/2}\right|+\epsilon}\right)^{r}. \tag{3.14}$$

$\epsilon=10^{-16}$ is a small constant to prevent division by zero. The value of r is chosen as equal to 6 to enhance sensitivity to both smooth and non-smooth regions. This function employs the local pressure ratio to assess local variations and identify the abrupt change near discontinuities. However, in order to detect contact discontinuity, one may also construct Eq. (3.14) using density. It is evident that $s_{\psi,i}\leq 1$ and $s_{\psi,i}=\mathcal{O}\left(\Delta x^{6}\right)$ in a smooth region of the flow. Consequently, we characterize the local smoothness at x_i as

$$s_i=\max\left(s_{\rho,i},s_{p,i}\right), \tag{3.15}$$

and at the interface $x_{i+1/2}$, it can be calculated as

$$s_{i+1/2}=\max(s_i,s_{i+1}). \tag{3.16}$$

Now, introducing two free parameters, that can be expressed in linear form as

$$\xi(s_{i+1/2}) = \widetilde{\alpha} - \widetilde{\beta} s_{i+1/2}. \tag{3.17}$$

It is clear that the value of ξ is dependent on $\widetilde{\alpha}$ and $\widetilde{\beta}$. We set $\widetilde{\alpha}=1/55$ and $\widetilde{\beta}=4$, and these values were chosen following the execution of numerous numerical experiments. These values remain unchanged for all the numerical simulations. Nevertheless, the actual dependency of these constants on ξ needs further analysis. In section 4.5.2, we demonstrate the impact of the value of $\widetilde{\alpha}$ on the final solution. Note that the anti-diffusive flux must vanish in the vicinity of the discontinuity. Hence, the anti-diffusive coefficient at the cell interface $\lambda_{1,i+1/2}$ is defined as

$$\lambda_{1,i+1/2} = \max(0,\xi). \tag{3.18}$$

When the value of $s_{i+1/2}$ is small, the solution is smooth, which activates the anti-diffusion and significantly reduces the numerical dissipation. On the other hand, if the value of $s_{i+1/2}$ is large, then the region contains a discontinuity that returns zero anti-diffusion. In this way, we constructed the local adaptive artificial anti-diffusion that aids in resolving the high wave number scales in the smooth region. Considering the robustness and necessary conditions of the scheme, we implement this anti-diffusion in the reconstruction procedure. Nonetheless, this can also be executed during the flux-splitting procedure. However, in this case, it may imply a violation of the necessary condition of the scheme and modify the flux splitting process. Thus, Eq. (3.10) can be reformulated by incorporating the anti-diffusive function $\left(u^*_{i+1/2}\right)$ as

$$\begin{aligned}\hat{u}^*_{i+1/2} = \frac{1}{12}(-u_{i-1}+7u_i+7u_{i+1}-u_{i+2}) \\ -\phi^*\left(\Delta u^+_{i-3/2},\Delta u^+_{i-1/2},\Delta u^+_{i+1/2},\Delta u^+_{i+3/2},\lambda^+_{1,i+1/2}\right) \qquad (3.19)\\ +\phi^*\left(\Delta u^-_{i+5/2},\Delta u^-_{i+3/2},\Delta u^-_{i+1/2},\Delta u^-_{i-1/2},\lambda^-_{1,i+1/2}\right), \qquad (3.20)\end{aligned}$$

where

$$\phi^*(a,b,c,d,r) = \frac{1}{3}\omega_2(a-2b+c) + \frac{1}{6}\left(\omega_1 - \frac{1}{2} + 6r\right)(b-2c+d). \tag{3.21}$$

ϕ^* is the modified dissipation function. The flux at the cell interface, $x_{i+1/2}$, can be defined as

$$\widetilde{f}_{i+1/2} = f\left(\hat{u}^*_{i+1/2}\right). \tag{3.22}$$

3.2 Enforcing fourth-order central difference in highly smooth region

In the second strategy, to enforce the fourth-order central difference scheme in the very smooth region, another adaptive coefficient is introduced in Eq. (3.19), which is given as

$$\begin{aligned}\hat{u}^*_{i+1/2} = \frac{1}{12}(-u_{i-1}+7u_i+7u_{i+1}-u_{i+2}) \\ -\lambda_{2,i+1/2}\phi^*\left(\Delta u^+_{i-3/2},\Delta u^+_{i-1/2},\Delta u^+_{i+1/2},\Delta u^+_{i+3/2},\lambda^+_{1,i+1/2}\right) \\ +\lambda_{2,i+1/2}\phi^*\left(\Delta u^-_{i+5/2},\Delta u^-_{i+3/2},\Delta u^-_{i+1/2},\Delta u^-_{i-1/2},\lambda^-_{1,i+1/2}\right),\end{aligned} \tag{3.23}$$

The value of $\lambda_{2,i+1/2}$ is switched in binary manner as

$$\lambda_{2,i+1/2} = \begin{cases} 0, & \text{if } s_{i+1/2} < 10^{-6}, \\ 1, & \text{otherwise,} \end{cases} \tag{3.24}$$

and

$$\lambda_{1,i+1/2} = 0, \quad \text{if } \lambda_{2,i+1/2} = 0. \tag{3.25}$$

The condition (3.25) ensures that there will be no numerical diffusion and artificial anti-diffusion in the highly smooth region. This enforcement would reduce the order of accuracy to fourth to enhance the resolution of the overall scheme. Note that the TENO5 scheme would converge to the fifth-order linear scheme in this region. The numerical dissipation of this fifth-order linear scheme is eliminated by forcing the central difference scheme.

To prevent scheme degradation at the critical point, where the first derivative is zero and the third derivative is non-zero, an additional condition is integrated into the scheme as

$$\lambda_{2,i+1/2} = 0, \quad \text{if } \Delta u_{i+1/2}\Delta u_{i-1/2} \le 0. \tag{3.26}$$

3.3 Variable C_T value

It is proven that the magnitude of C_T has a significant influence on the spectral characteristics of the scheme. In the TENO5A scheme, the value of C_T is reduced in the smooth region, along with the numerical errors. However, we relax this variation slightly due to the adaptation of anti-dissipation, which already contributes to dropping numerical diffusion. The local smoothness is measured using an alternative sensor [30], defined as

$$\sigma_{i+1/2} = 1 - \min\left(1, \frac{\Phi_{i+1/2}}{\Phi_c}\right), \tag{3.27}$$

where

$$\Phi_{i+1/2} = \min(\Phi_{i-1}, \Phi_i, \Phi_{i+1}), \tag{3.28}$$

$$\Phi_i = \frac{2ab+\zeta}{a^2+b^2+\zeta}, \tag{3.29}$$

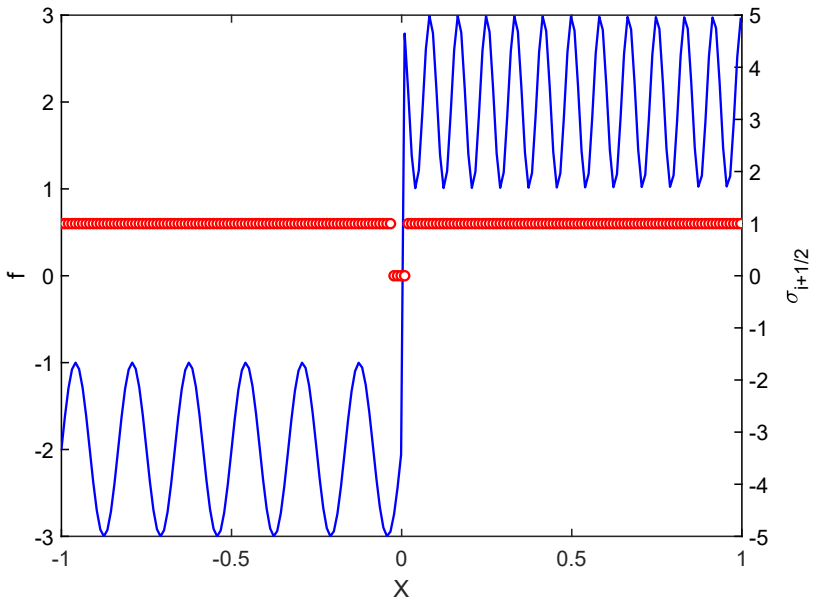

Figure 2: Distribution of $\sigma_{i+1/2}$ (red circles) for Eq. (3.31) (solid line) with $N=192$ on uniform grid.

and

$$\begin{aligned} a &= |u_i - u_{i-1}| + |u_{i-2} - 2u_{i-1} + u_i|, \\ b &= |u_{i+1} - u_i| + |u_i - 2u_{i+1} + u_{i+2}|, \\ \zeta &= \frac{0.9\Phi_c}{1-0.9\Phi_c}\theta^2, \\ \theta &= 10^{-3}, \quad \Phi_c = 0.25. \end{aligned} \tag{3.30}$$

Introducing the second derivative in the expression of a and b increases the sensitivity to shock. Near the discontinuity, the second-order derivative will have an abrupt change, which improves the detection of the discontinuity. Conversely, in proximity to the local extrema, the first-order derivative will be high, while the variation of the second-order derivative is not very large [30]. This helps to prevent any false detection. For testing this detector, we use the following function

$$f = \begin{cases} \sin(12\pi x) - 2, & \text{if } -1 \le x < 0, \\ \sin\left(24\pi x + \frac{\pi}{2}\right), & \text{if } 0 \le x \le 1. \end{cases} \tag{3.31}$$

Fig. 2 shows the accuracy of the shock detector for a function with shock and smooth regions. It is evident that the discontinuity detector is highly sensitive to the shock and avoids false detection. The parameter C_T varies according to the value of $\sigma_{i+1/2}$ as defined by the function

$$C_T(\sigma_{i+1/2}) = 10^{\Omega(\sigma_{i+1/2})}. \tag{3.32}$$

The variation of $\Omega(\sigma_{i+1/2})$ is given as

$$\begin{aligned}\Omega(\sigma_{i+1/2}) =& 8(\Psi(\sigma_{i+1/2},0.2)) + 7(\Psi(\sigma_{i+1/2},0.4) - \Psi(\sigma_{i+1/2},0.2)) \\ &+ 6(\Psi(\sigma_{i+1/2},0.6) - \Psi(\sigma_{i+1/2},0.4)) - 5(1 + \Psi(\sigma_{i+1/2},0.6)),\end{aligned} \tag{3.33}$$

where the function $\Psi(\sigma_{i+1/2},\text{lim})$ is defined as

$$\Psi(\sigma_{i+1/2},\text{lim}) = \min\Big(1,\min(\lfloor \sigma_{i+1/2}/\text{lim} \rfloor - 1,0)\Big). \tag{3.34}$$

Eq. (2.10) is rewritten as

$$\delta_k = \begin{cases} 0, & \text{if } \chi_k < C_T(\sigma), \\ 1, & \text{otherwise.} \end{cases} \tag{3.35}$$

The subsequent steps outline the estimation of $\hat{u}^*_{i+1/2}$ as presented in Eq. (3.23):

Step 1: Assessing the value of $\lambda^{\pm}_{1,i+1/2}$ using Eq. (3.18) by predicting the local field fluctuation utilising the switching function presented in Eq. (3.14).

Step 2: Determining the value of $\lambda^{\pm}_{2,i+1/2}$ in accordance with Eq. (3.24). This value fluctuates in a binary manner based on the local smoothness.

Step 3: The expression for ϕ^* is provided in Eq. (3.21), and the TENO weights ω_1 and ω_2 are determined by adhering to the procedure outlined in Eq. (2.6) through Eq. (2.11), with the exception that Eq. (2.10) is replaced with Eq. (3.35).

Remark 3.1. The magnitudes of $\lambda_{1,i+1/2}$ and $\lambda_{2,i+1/2}$ are solely determined from $s_{i+1/2}$ given in Eq. (3.16).

Remark 3.2. In a section of flow that is exceedingly smooth or uniform, both $\lambda_{1.i+1/2}$ and $\lambda_{2,i+1/2}$ will equal zero, necessitating the application of a fourth-order central difference scheme throughout the reconstruction process. The value of Ω will be -8, which guarantees a low C_T. Nonetheless, the TENO reconstruction is not applicable in this instance, rendering the value of Ω inconsequential.

Remark 3.3. If the region is smooth with multi-scale structures, then the anti-diffusion will be activated and the value of $\lambda_{1,i+1/2}$ will be evaluated from Eq. (3.18). The value of $\lambda_{2,i+1/2}$ will equal one. The value of Ω will be varied based on the response of the shock detector (Eq. (3.27)).

Remark 3.4. In a flow zone containing a shock wave, the value of $s_{i+1/2}$ will be elevated, and $\lambda_{1,i+1/2}$ will equal zero. The value of Ω will be -5, indicating that the standard TENO5 reconstruction will be utilised for flux reconstruction.

3.4 Consistency and convergence

The anti-diffusive term at the interface in Eq. (3.13) can be written as

$$u^*_{i+1/2} = \lambda_{1,i+1/2}(\Delta u_{i+3/2} - 2\Delta u_{i+1/2} + \Delta u_{i-1/2}). \tag{3.36}$$

The Taylor series expansion of Eq. (3.36) is

$$u^*_{i+1/2} = \lambda_{1,i+1/2}\left(\Delta x^3 u''' + \frac{\Delta x^4 u^{(iv)}}{2} + \mathcal{O}(\Delta x^5)\right). \tag{3.37}$$

Hence,

$$\begin{aligned} &u^*_{i+1/2} - u^*_{i-1/2} \\ &= (\lambda_{1,i+1/2} - \lambda_{1,i-1/2})\Delta x^3 u''' + (\lambda_{1,i+1/2} + \lambda_{1,i-1/2})\frac{\Delta x^4 u^{iv}}{2} + \mathcal{O}(\Delta x^5). \end{aligned} \tag{3.38}$$

Therefore, in the smooth region of a flow, the anti-diffusion converges as

$$u^*_{i+1/2} - u^*_{i-1/2} = \mathcal{O}(\Delta x^3) \quad \text{and} \quad \lambda_{1,k} = \mathcal{O}(1). \tag{3.39}$$

Hence, the anti-diffusion term in Eq. (3.12) vanishes as $\Delta x \to 0$, so ensuring consistency. In a smooth region, the magnitude of $s_{i+1/2}$ in Eq. (3.17) becomes zero and ξ converges to $\widetilde{\alpha}$. At discontinuities, the value of $s_{i+1/2}$ is large and $\lambda_{1,i+1.2}$ will be zero. If $\lambda_{1,i+1/2} = \lambda_{1,i-1/2}$, then the anti-diffusion terms will exhibit fourth-order accuracy with a coefficient of $\lambda_{1,k}\Delta x^3$.

3.5 Spectral property

The spectral characteristics of the proposed scheme are studied by using Approximate Dispersion Relation (ADR) [31]. The numerical dispersion and dissipation are quantified through the Real ($\Re(\Phi)$) and imaginary ($\Im(\Phi)$) parts of the modified wavenumber Φ. The spectral properties of the different schemes are shown in Fig. 3. The TENO5A scheme has much less numerical dissipation than the standard TENO5 scheme, and its spectral characteristics align with those of a fifth-order linear central upwind biased scheme. It is observed that the proposed scheme shows a significant reduction in numerical diffusion compared to the standard TENO5 and TENO5A schemes, especially in the intermediate wavenumbers. It is also shown that the magnitude of $\widetilde{\alpha}$ has considerable influence on the spectral property of the proposed scheme. The in-built numerical dissipation is further attenuated with the value of $\widetilde{\alpha}$, however, to maintain stability and robustness, we set it as $1/55$.

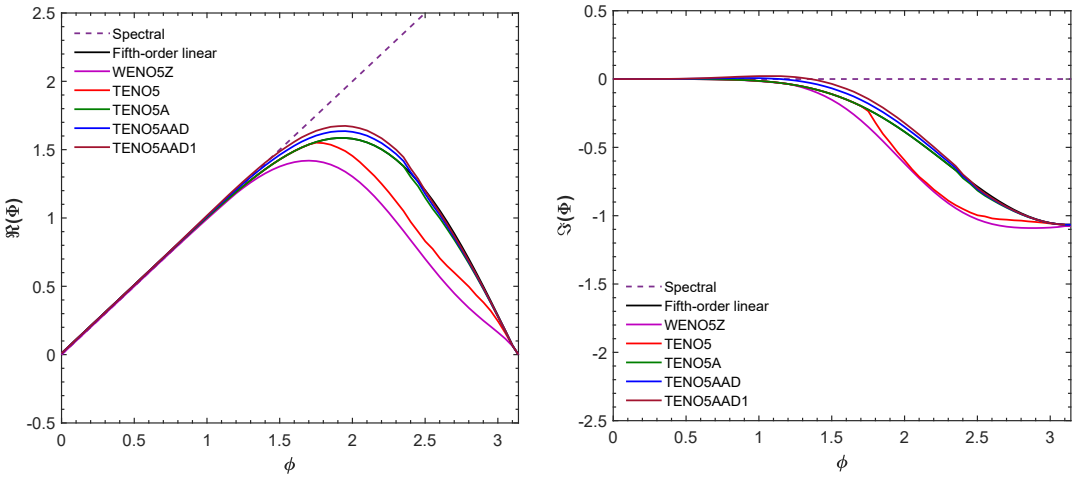

Figure 3: Approximate Dispersion Relation (ADR) of WENO5Z, TENO5, TENO5A and present scheme. The present scheme is shown with $\widetilde{\alpha}=1/55$ (TENO5AAD) and $\widetilde{\alpha}=1/45$ (TENO5AAD1).

4 Numerical validation

This section assesses the efficacy of the present scheme using a set of numerical benchmark test cases. The compressible Euler and Navier-Stokes equations are solved within the finite volume framework. The ideal gas equation is incorporated to complete the system. For the system of conservation laws, the Roe average [32] is adopted for characteristic decomposition, and the Rusanov flux splitting solver [33] is employed for the convection terms to ensure up-winding at the cell interfaces. The Courant-Friedrichs-Lewy (CFL) number is set as 0.4 for one-dimensional problems and 0.6 for two-dimensional problems. Following the semi-discrete method, the resulting Ordinary Differential Equation (ODE) is advanced in time employing the low-storage third-order Strong Stability-Preserving (SSP) Runge-Kutta technique [34]. The numerical symmetric preserving techniques [35, 36] are deployed to prevent asymmetry in the solution due to floating point noise. The threshold parameter C_T for the TENO5 scheme is set as 10^{-5}.

4.1 Linear advection

We consider the one-dimensional linear advection equation

$$\frac{\partial f}{\partial t}+\frac{\partial f}{\partial x}=0. \tag{4.1}$$

The analytical solution of Eq. (4.1) is given by

$$f_{ex}=f_{in}(x-t), \tag{4.2}$$

where f_{in} is the initial solution at time $t=0$.

The error norms are computed by

$$\begin{aligned} L_1 &= \frac{2}{N}\sum_{i=0}^{N}|f_i - f_{ex,i}|, \\ L_2 &= \sqrt{\frac{2}{N}\sum_{i=0}^{N}(f_i - f_{ex,i})^2}, \\ L_\infty &= \max|f_i - f_{ex,i}| \quad \text{for} \quad i = 0,\dots,N. \end{aligned} \tag{4.3}$$

4.1.1 Linear advection of sine function

This test case is intended to analyze the rate of convergence of the proposed scheme. Eq. (4.1) is solved with the initial condition

$$f(x,0) = \sin\left(\pi x - \frac{\sin(\pi x)}{\pi}\right) \quad \text{on} \quad x \in [-1,1]. \tag{4.4}$$

The initial solution is advanced to $t = 2$. Periodic boundary conditions are applied to the left and right boundaries of the domain. The given function possesses two critical points, one at $x = -0.6$ and the other at $x = 0.6$, where the first derivative is zero, while the third derivative is non-zero. The exact solution of Eq. (4.4) is given as

$$f_{ex}(x,t) = \sin\left(\pi(x-t) - \frac{\sin(\pi(x-t))}{\pi}\right). \tag{4.5}$$

Tables 1-4 show the convergence statistics of the L_1, L_2 and L_∞ norms of WENO5Z, TENO5, TENO5A and TENO5AAD schemes. It is proven that the proposed scheme converges to fifth-order accuracy in the presence of critical points.

Table 1: Convergence statistics of WENO5Z.

N	L_1 norm	r_c	L_2 norm	r_c	L_∞ norm	r_c	Elapsed time [s]
50	4.36E-05	-	3.94E-05	-	5.58E-05	-	0.003367
100	1.37E-06	4.99	1.24E-06	4.993	1.74E-06	4.998	0.00955
200	4.30E-08	5.00	3.88E-08	4.997	5.46E-08	4.999	0.03148
400	1.34E-09	5.00	1.21E-09	4.999	1.70E-09	5.00	0.16857
800	4.21E-11	5.00	3.79E-11	4.997	5.48E-11	4.958	0.80862
1600	1.32E-12	5.00	1.19E-12	5.00	1.74E-12	4.979	4.86416

Table 2: Convergence statistics of TENO5.

N	L_1 norm	r_c	L_2 norm	r_c	L_∞ norm	r_c	Elapsed time [s]
50	4.36E-05	-	3.94E-05	-	5.58E-05	-	0.00837
100	1.37E-06	4.991	1.24E-06	4.993	1.74E-06	4.997	0.03690
200	4.30E-08	4.995	3.88E-08	4.996	5.46E-08	4.999	0.21147
400	1.34E-09	4.998	1.21E-09	4.999	1.70E-09	5.000	1.12272
800	4.21E-11	4.997	3.79E-11	4.997	5.48E-11	4.958	4.78981
1600	1.32E-12	4.999	1.19E-12	5.000	1.74E-12	4.976	23.35703

Table 3: Convergence statistics of TENO5A.

N	L_1 norm	r_c	L_2 norm	r_c	L_∞ norm	r_c	Elapsed time [s]
50	4.36E-05	-	3.94E-05	-	5.58E-05	-	0.011534
100	1.37E-06	4.991	1.24E-06	4.993	1.74E-06	4.997	0.053429
200	4.30E-08	4.995	3.88E-08	4.996	5.46E-08	4.999	0.32914
400	1.34E-09	4.998	1.21E-09	4.999	1.70E-09	5.000	2.05831
800	4.21E-11	4.997	3.79E-11	4.997	5.48E-11	4.958	5.98035
1600	1.32E-12	4.999	1.19E-12	5.000	1.74E-12	4.976	35.40683

Table 4: Convergence statistics of TENO5AAD.

N	L_1 norm	r_c	L_2 norm	r_c	L_∞ norm	r_c	Elapsed time [s]
50	4.36E-05	-	3.95E-05	-	5.58E-05	-	0.01265
100	1.37E-06	4.991	1.23E-06	4.993	1.75E-06	4.997	0.06729
200	4.30E-08	4.995	3.88E-08	4.996	5.46E-08	4.999	0.39448
400	1.34E-09	4.998	1.21E-09	4.999	1.70E-09	5.000	2.38392
800	4.21E-11	4.997	3.79E-11	4.997	5.48E-11	4.958	6.83922
1600	1.32E-12	4.999	1.19E-12	5.000	1.74E-12	4.976	40.42565

4.1.2 Linear advection of multiple waves

We consider the test case proposed in [11]. The initial condition is

$$f(x,0)=\begin{cases}\frac{1}{6}[G(x-1,\beta,z-\theta)+G(x-1,\beta,z+\theta)+4G(x-1,\beta,z)], & \text{if } 0.2\le x<0.4,\\ 1, & \text{if } 0.6\le x\le 0.8,\\ 1-|10(x-1.1)|, & \text{if } 1.0\le x\le 1.2,\\ \frac{1}{6}[F(x-1,\alpha,a-\theta)+F(x-1,\alpha,\alpha+\theta)+4F(x-1,\alpha,a)], & \text{if } 1.4\le x<1.6,\\ 0, & \text{otherwise,}\end{cases} \tag{4.6}$$

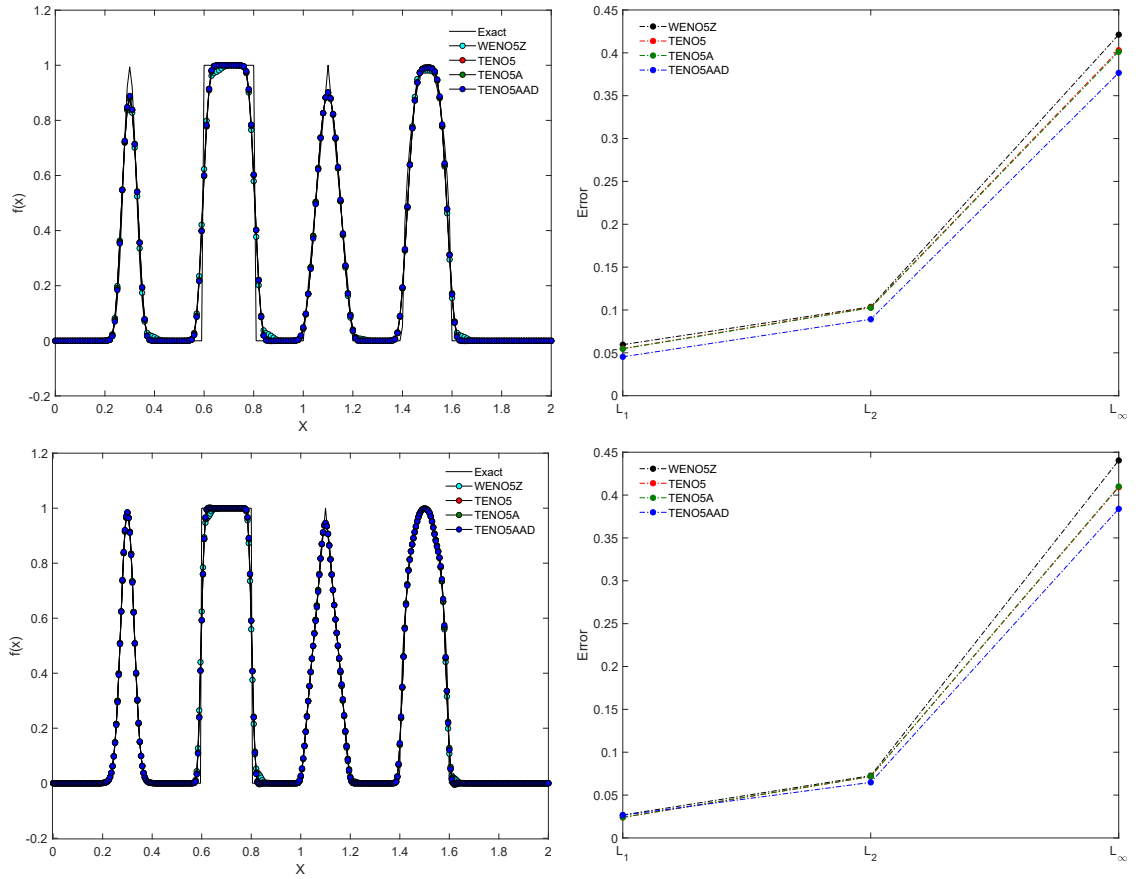

Figure 4: Linear advection of multiple waves: the left panel is the solution at $t=4$ and the right panel is the error norms. The top panel is for $N=200$ and the bottom panel is for $N=400$. The "Exact" is the analytical solution.

where

$$\begin{aligned} G(x,\beta,z) &= e^{-\beta(x-z)^2}, \\ F(x,\alpha,a) &= \sqrt{\max(1-\alpha^2(x-a)^2,0)}. \end{aligned} \tag{4.7}$$

The constants are $a=0.5, z=-0.7, \theta=0.005, \alpha=10$ and $\beta=\frac{\log 2}{36\theta^2}$. The computational domain is chosen in the interval $[0,2]$ and Eq. (4.1) is solved until the final simulation time $t=4$. Periodic boundary conditions are imposed on both boundaries. The final result and the L_1, L_2 and L_∞ norms of the proposed scheme are compared with the ones of the WENO5Z, TENO5 and the TENO5A schemes as shown in Fig. 4. It could be seen that the magnitude of the error norms of the current TENO5AAD scheme is less than that of the other schemes.

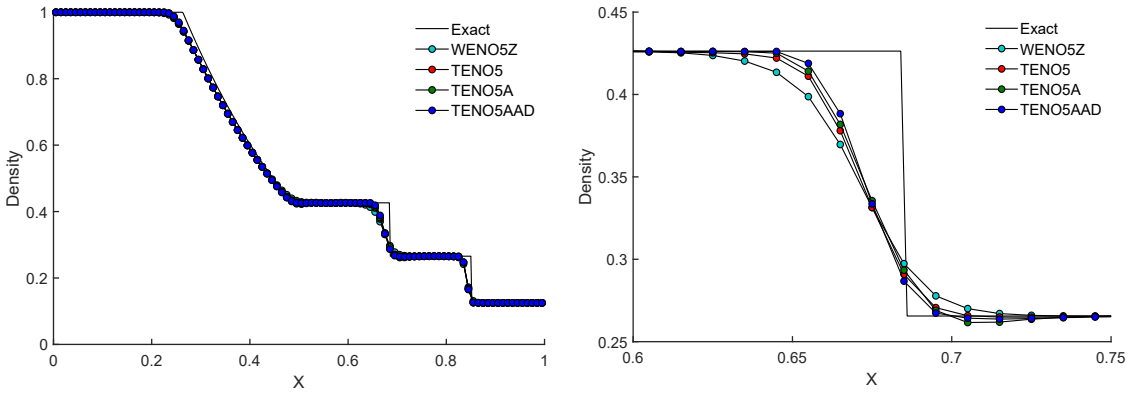

Figure 5: Sod shock tube problem: density distribution (left) and a zoomed-in view in the vicinity of the discontinuity (right) with a mesh resolution of $N=100$ at time $t=0.2$. The "Exact" represents the theoretical solution to the Riemann problem.

4.2 Shock tube problems

The Sod [37] and Lax [38] shock tube problems are executed to evaluate the shock-capturing capability of the current scheme. The initial condition for the Sod shock tube problem is

$$(\rho,u,p)=\begin{cases}(1,0,1), & \text{if } 0\le x<0.5,\\ (0.125,0,0.1), & \text{if } 0.5\le x\le 1,\end{cases} \tag{4.8}$$

and the final time of the simulation is $t=0.2$.
The initial condition of the Lax shock tube problem is

$$(\rho,u,p)=\begin{cases}(0.445,0.689,3.528), & \text{if } 0\le x<0.5,\\ (0.5,0,0.5710), & \text{if } 0.5\le x\le 1,\end{cases} \tag{4.9}$$

and the final time of the simulation is $t=0.14$. The density distributions of several schemes are compared with the exact theoretical solution of the Riemann problem. As shown in Fig. 5 and Fig. 6, the present TENO5AAD scheme captures the shock more sharply than the WENO5Z, TENO5 and TENO5A schemes. The current technique resolves the contact discontinuity more effectively than the other schemes, as demonstrated in the right panel of Fig. 5 and Fig. 6.

4.3 Interacting blast waves

The one-dimensional interaction of two blast waves from [39] is considered. The initial condition is

$$(\rho,u,p)=\begin{cases}(1,0,1000), & \text{if } 0\le x<0.1,\\ (1,0,0.01), & \text{if } 0.1\le x\le 0.9,\\ (1,0,100), & \text{if } 0.9\le x\le 1.\end{cases} \tag{4.10}$$

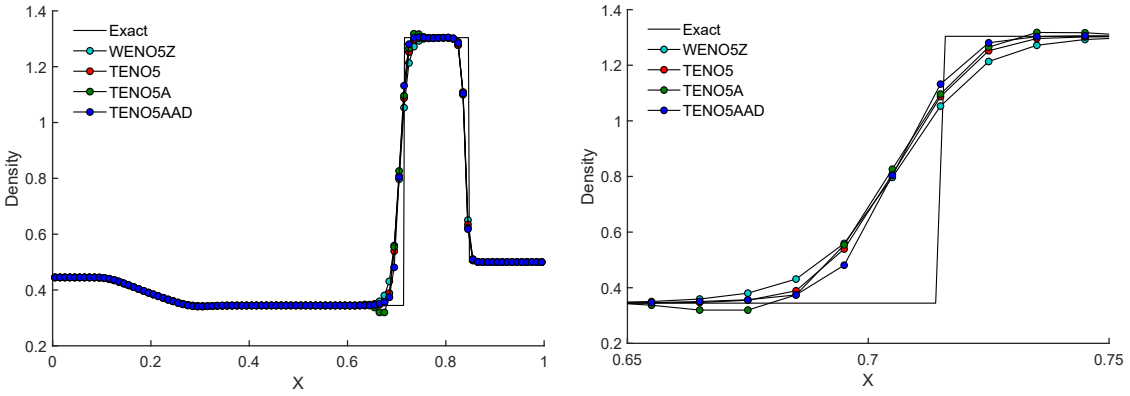

Figure 6: Lax shock tube problem: density distribution (left) and a zoomed-in view in the vicinity of the discontinuity (right) with a mesh resolution of $N=100$ at time $t=0.14$. The "Exact" represents the theoretical solution to the Riemann problem.

The simulation is performed until the time is $t=0.038$, with the boundaries configured as reflective. The reference solution is computed by the conventional fifth-order WENO-JS scheme with a resolution of $N=3000$ on a uniform mesh. Fig. 7 displays the spatial density distribution of different schemes at the final time. It is observed that the TENO5AAD outperforms the WENO5Z, TENO5 and TENO5A schemes in shock capturing and exhibits superior resolution of contact discontinuities relative to the other schemes.

4.4 Shock-density wave interaction

To assess the small-scale resolving nature of the current scheme, a perturbed density wave interacting with a shock wave of Mach number 3 is simulated. The initial condition is

$$(\rho,u,p)=\begin{cases}(3.857,2.629,10.333), & \text{if } -5\leq x<-4,\\ (1+0.2\sin(5x),0,1, & \text{if } -4\leq x\leq 5.\end{cases} \tag{4.11}$$

The final simulation time is $t=1.8$. The density distribution of various schemes is obtained and is illustrated in Fig. 8. The reference solution is produced by the conventional WENO-JS scheme with a mesh resolution of $N=3000$ and a uniform space interval. In comparison to other schemes, there is a remarkable improvement in the resolution of high-frequency density waves by the present TENO5AAD scheme.

4.5 2D Riemann problem

In order to verify the high-resolution capability of the numerical schemes, three classical 2D Riemann problems [40] of various configurations of discontinuities and multiscale structures are considered in this subsection.

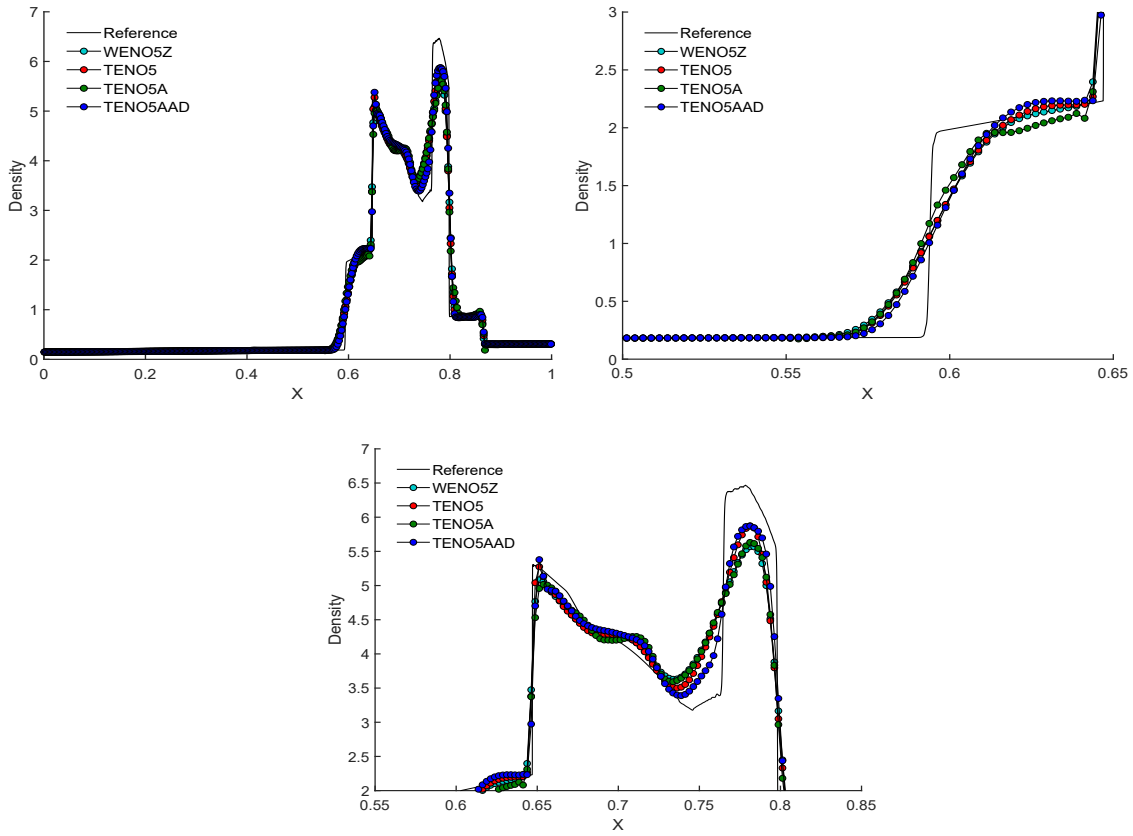

Figure 7: Interacting blast waves problem: density distribution (left) and a zoomed-in view in the vicinity of the discontinuity (right and bottom) with a mesh resolution of $N=400$ at time $t=0.038$. The "Reference" solution is computed using the WENO-JS scheme with a mesh resolution of $N=3000$.

4.5.1 Configuration 12

The initial condition is

$$(\rho,u,v,p)=\begin{cases}(0.5313,0,0,0.4), & \text{if } x>0.5,\ y>0.5,\\ (1,0.7276,0,1), & \text{if } x<0.5,\ y>0.5,\\ (0.8,0,0,1), & \text{if } x<0.5,\ y<0.5,\\ (1,0,0.7276,1), & \text{if } x>0.5,\ y<0.5.\end{cases} \tag{4.12}$$

The computational domain is defined as $[0,1]\times[0,1]$, with a final simulation time of $t=0.25$. Fig. 9 shows the density distribution of the different schemes in $[0.2,0.6]\times[0.2,0.6]$. The small vortex structures are better resolved by the TENO5AAD scheme than the WENO5Z, TENO5 and TENO5A schemes, owing to its minimal numerical dissipation regulated by adaptive anti-diffusion.

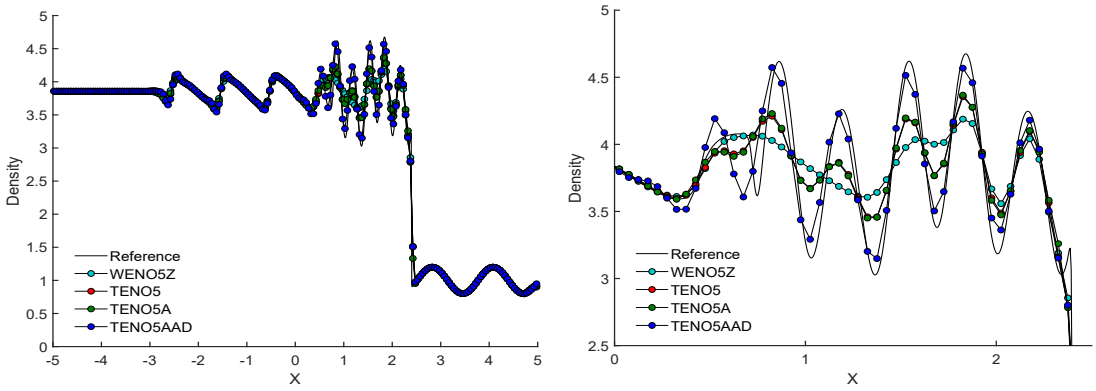

Figure 8: Shock-density wave interaction problem: density distribution (left) and a zoomed-in view in the vicinity of the discontinuity (right) with a mesh resolution of $N=200$ at time $t=1.8$. The "Reference" solution is computed using the WENO-JS scheme with a mesh resolution of $N=3000$.

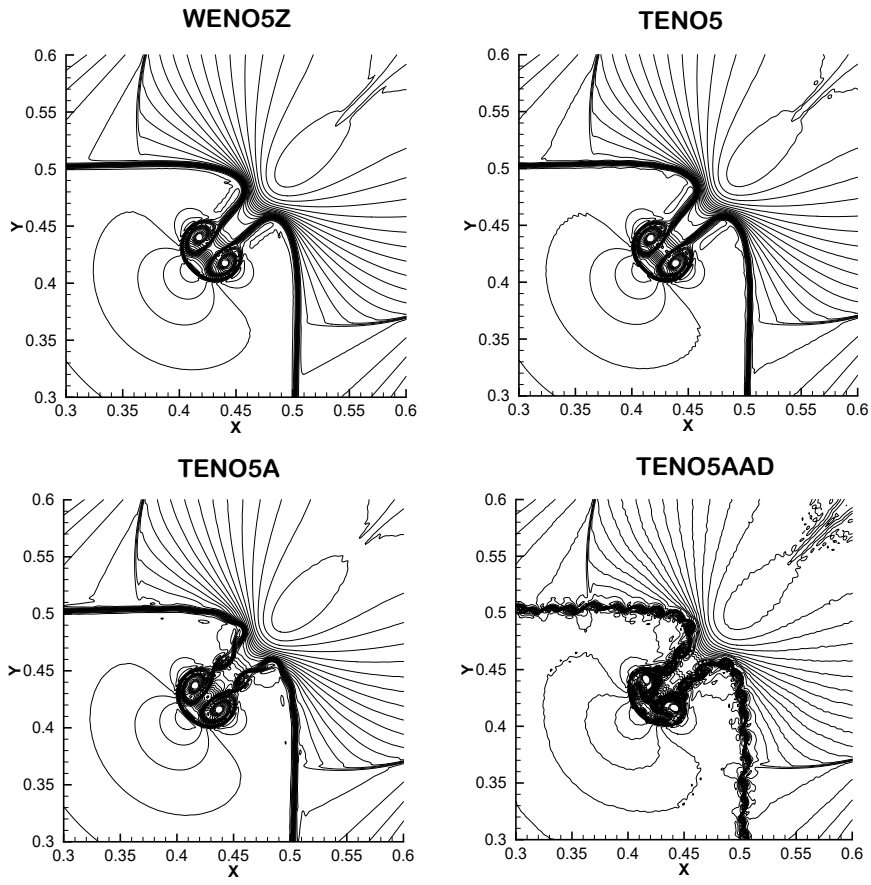

Figure 9: 2D Riemann problem (configuration 12): density distributions with 45 contour lines from 0.75 to 1.5. Mesh resolution is 1024×1024.

4.5.2 Configuration 8

The initial condition is

$$(\rho,u,v,p)=\begin{cases}(0.5197,0.1,0.1,0.4), & \text{if } x>0.5,\ y>0.5,\\ (1,-0.6259,0.1,1), & \text{if } x<0.5,\ y>0.5,\\ (0.8,0.1,0.1,1), & \text{if } x<0.5,\ y<0.5,\\ (1,0.1,-0.6259,1), & \text{if } x>0.5,\ y<0.5.\end{cases} \tag{4.13}$$

The computational domain is defined as $[0,1]\times[0,1]$, with a final simulation time of $t=0.25$. While comparing the schemes, the present scheme captures shock sharply and resolves much vortical structure due to the alleviation of intrinsic numerical dissipation by the anti-diffusion as shown in Fig. 10. The influence of $\widetilde{\alpha}$ in Eq. (3.17) is demonstrated

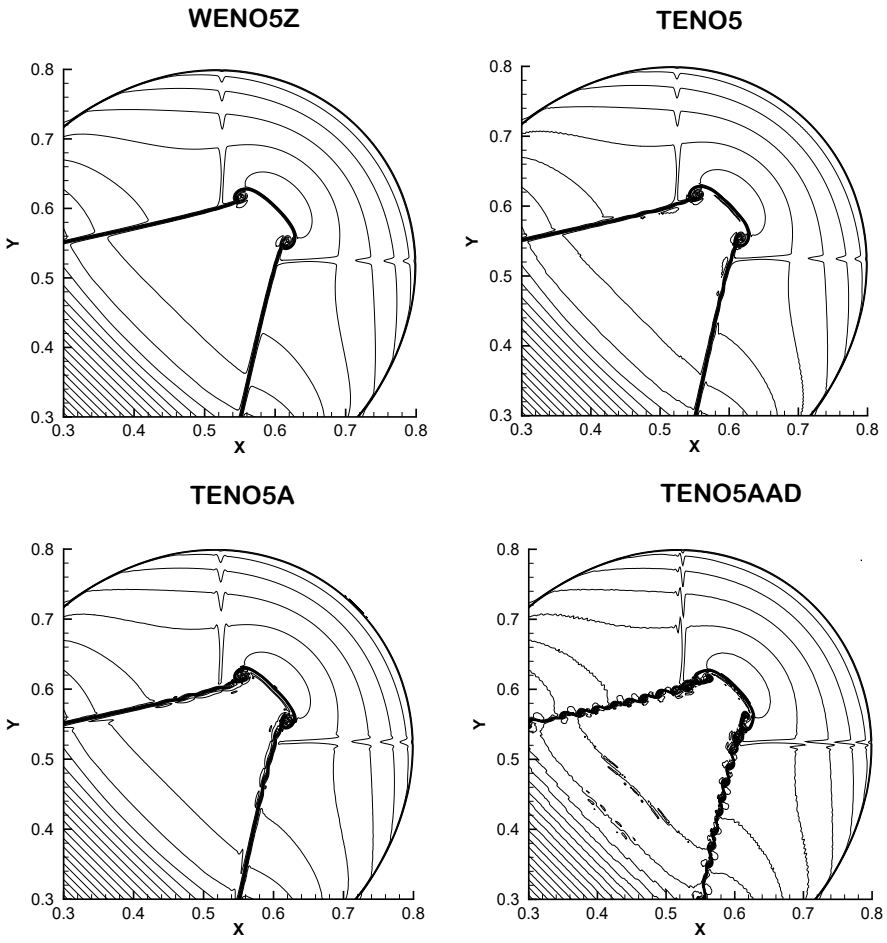

Figure 10: 2D Riemann problem (configuration 8): density distributions with 35 contour lines from 0.4 to 0.9. Mesh resolution is 1024×1024.

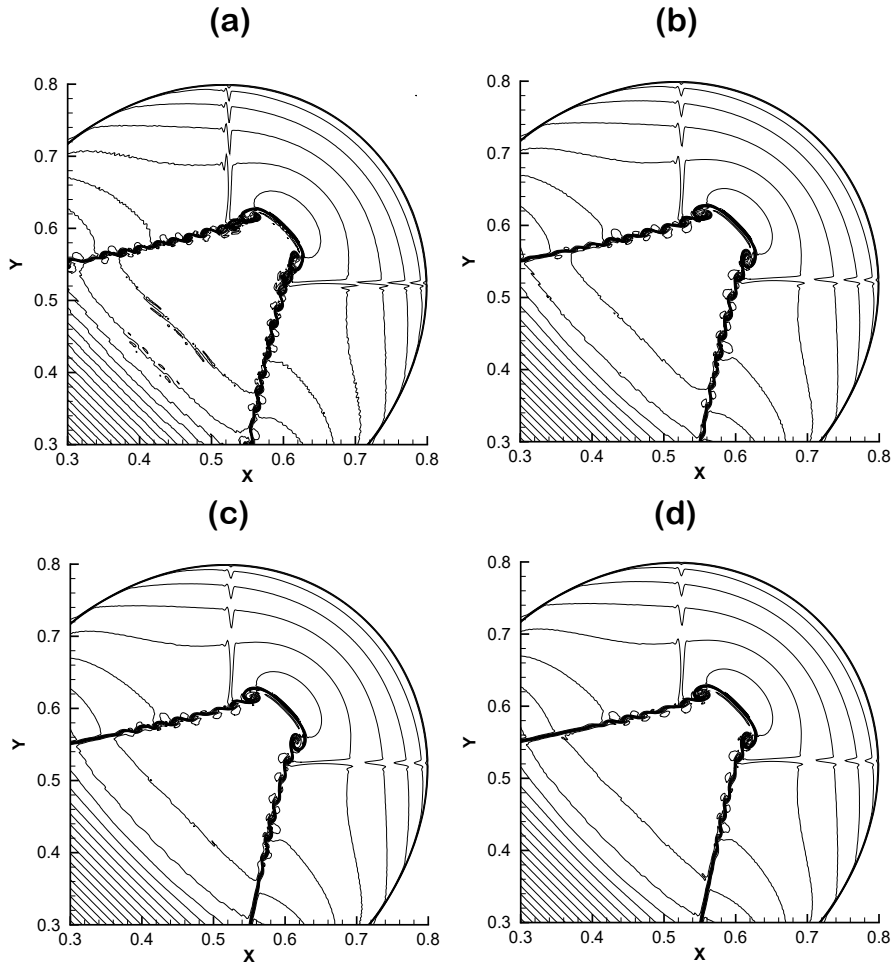

Figure 11: 2D Riemann problem (configuration 8): density distributions of the TENO5AAD scheme with (a) $\widetilde{\alpha}=1/55$, (b) $\widetilde{\alpha}=1/100$, (c) $\widetilde{\alpha}=1/150$, (d) $\widetilde{\alpha}=1/200$.

in Fig. 11. It can be clearly seen that the effect of anti-diffusion diminishes as the magnitude of $\widetilde{\alpha}$ reduces.

4.5.3 Configuration 11

The initial condition is

$$(\rho,u,v,p)=\begin{cases}(1,0.1,0,1), & \text{if } x>0.5,\ y>0.5,\\ (0.5313,0.8276,0,0.4), & \text{if } x<0.5,\ y>0.5,\\ (0.8,0.1,0,0.4), & \text{if } x<0.5,\ y<0.5,\\ (0.5313,0.1,0.7276,0.4), & \text{if } x>0.5,\ y<0.5.\end{cases} \tag{4.14}$$

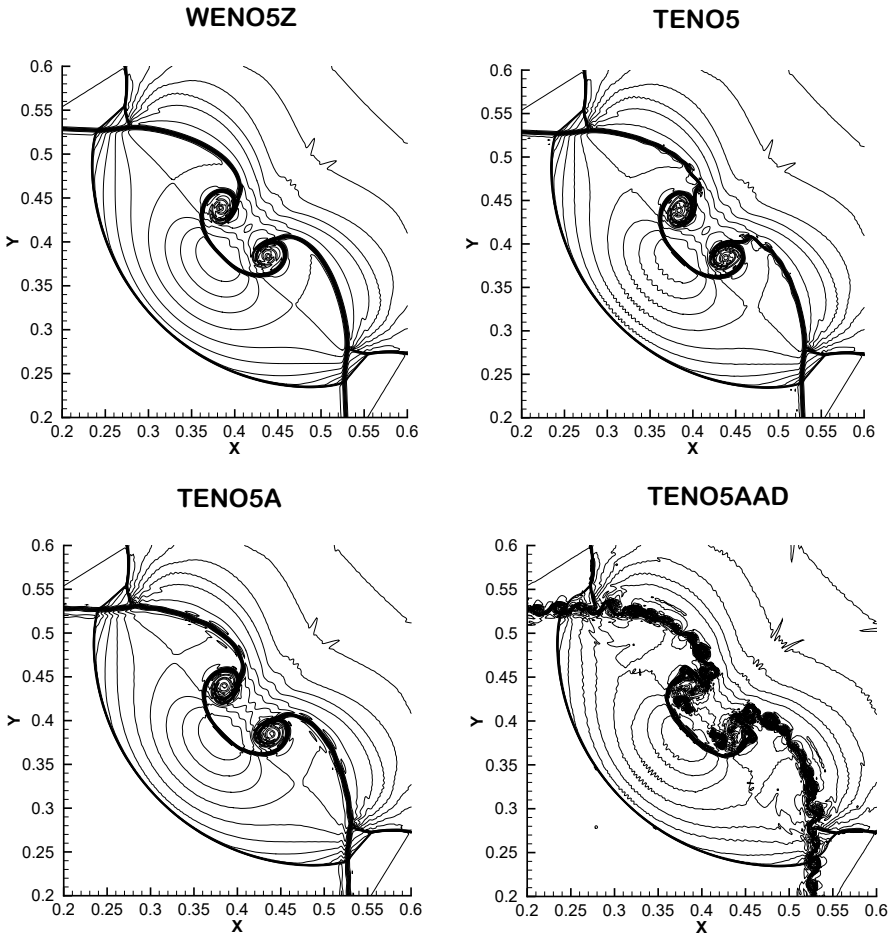

Figure 12: 2D Riemann problem (configuration 11): density distributions with 30 contour lines from 0.4 to 1.2. Mesh resolution is 1024×1024.

The computational domain is defined as $[0,1]\times[0,1]$, with a final simulation time of $t=0.3$. The density distribution at the final simulation time for the WENO5Z, TENO5, TENO5A and TENO5AAD schemes is shown in Fig. 12. The present scheme outperforms the remaining ones in terms of stable shock-capturing ability and resolving fine structures, signifying less numerical dissipation.

4.6 Kelvin-Helmholtz instability

The Kelvin-Helmholtz instability presented in [27] is considered. The initial condition is given by

$$(\rho,u)=\begin{cases}(2,-0.5), & \text{if } |y|<0.25,\\ (1,0.5), & \text{otherwise,}\end{cases} \tag{4.15}$$

and

$$(v,p) = (0.01\sin(2\pi x), 2.5). \tag{4.16}$$

The computational domain is $[-0.5,0.5]\times[-0.5,0.5]$., and the total simulation duration is $t=1$. Periodic boundary conditions are enforced on all boundaries of the domain. The density distributions and the time evolution of the normalized total kinetic energy are shown in Fig. 13. It is observed that the TENO5AAD scheme could capture more small vortical structures than the other compared schemes and trigger the vortex pairing rigorously. It is also worth noting that the present scheme performs better in preserving the total kinetic energy of the flow due to its low numerical dissipation, which is enhanced by the adaptive artificial anti-diffusion.

4.6.1 Rayleigh-Taylor instability

The inviscid Rayleigh-Taylor instability is examined, encompassing both discontinuities and intricate flow configurations as detailed in [18]. The size of the computational domain is $[0,0.25]\times[0,1]$ in the x and y directions. The initial states are given as

$$(\rho,u,v,p) = \begin{cases} (2,0,-0.025c\cdot\cos(8\pi x),1+2y), & \text{if } y<0.5, \\ (1,0,-0.025c\cdot\cos(8\pi x),y+3/2), & \text{if } y\geq 0.5, \end{cases} \tag{4.17}$$

where $\gamma=\frac{5}{3}$ and $c=\sqrt{\frac{\gamma p}{\rho}}$ represents the speed of sound. The upper and lower boundaries adhere to Dirichlet boundary conditions, with the primitive variables (ρ,u,v,p) set as $(1,0,0,2.5)$ and $(2,0,0,1)$ respectively. The left and right boundaries are set as symmetric. Initially, the low and high-density fluids are separated by the interface. The denser fluid is propelled by gravity; hence, a source term is incorporated into the y-momentum and energy equations as ρ and ρv. The grid spatial interval is chosen as $\Delta x=\Delta y=1/512$. The final simulation time is $t=1.95$.

The density distribution at the final simulation time of the WENO5Z, TENO5, TENO5A and TENO5AAD schemes at the mesh resolution of 128×512 is given in Fig. 14. It is clear that the TENO5AAD scheme has resolved much smaller-scale structures than the other higher-order schemes. It should also be noted that the flow symmetry is maintained in the present scheme. Fig. 15 demonstrates the y-direction energy spectrum at the final time of various schemes. It is worth mentioning that the energy distribution of the proposed scheme at small length scales is more energetic than that of the other schemes. The spectrum of the TENO5AAD scheme with a coarse mesh is marginally superior to that of the TENO5 scheme with a fine mesh. Table 5 exhibits the statistics of computational cost in terms of computational time per unit iteration for WENO5Z, TENO5, TENO5A and TENO5AAD schemes. It is evident that the computational effort of the present scheme is about equivalent to that of the TENO5A scheme.

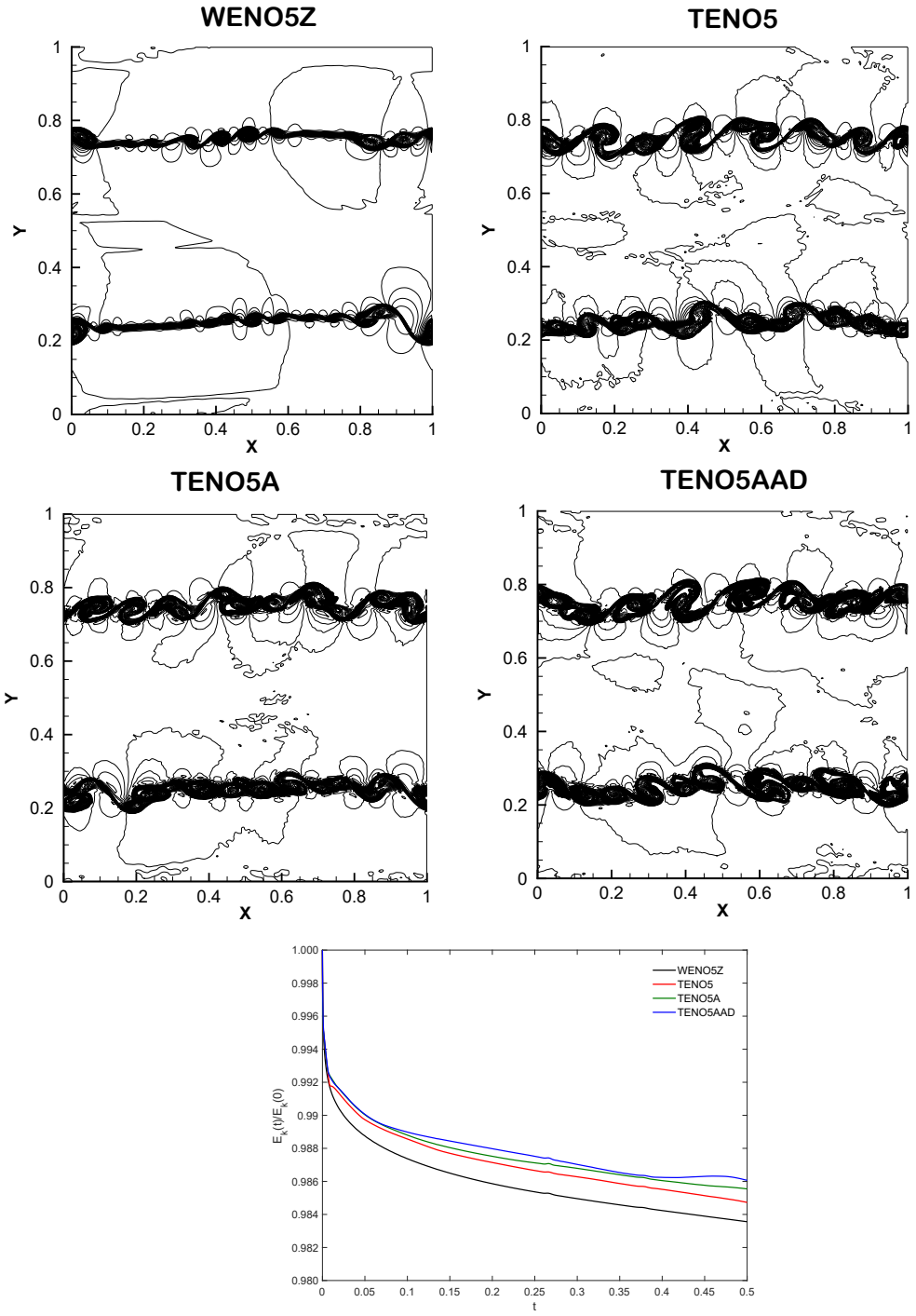

Figure 13: Kelvin-Helmholtz instability: density distributions with 45 contours from 1 to 2.1. Mesh resolution is 512×512. Bottom: the time evolution of normalized total kinetic energy.

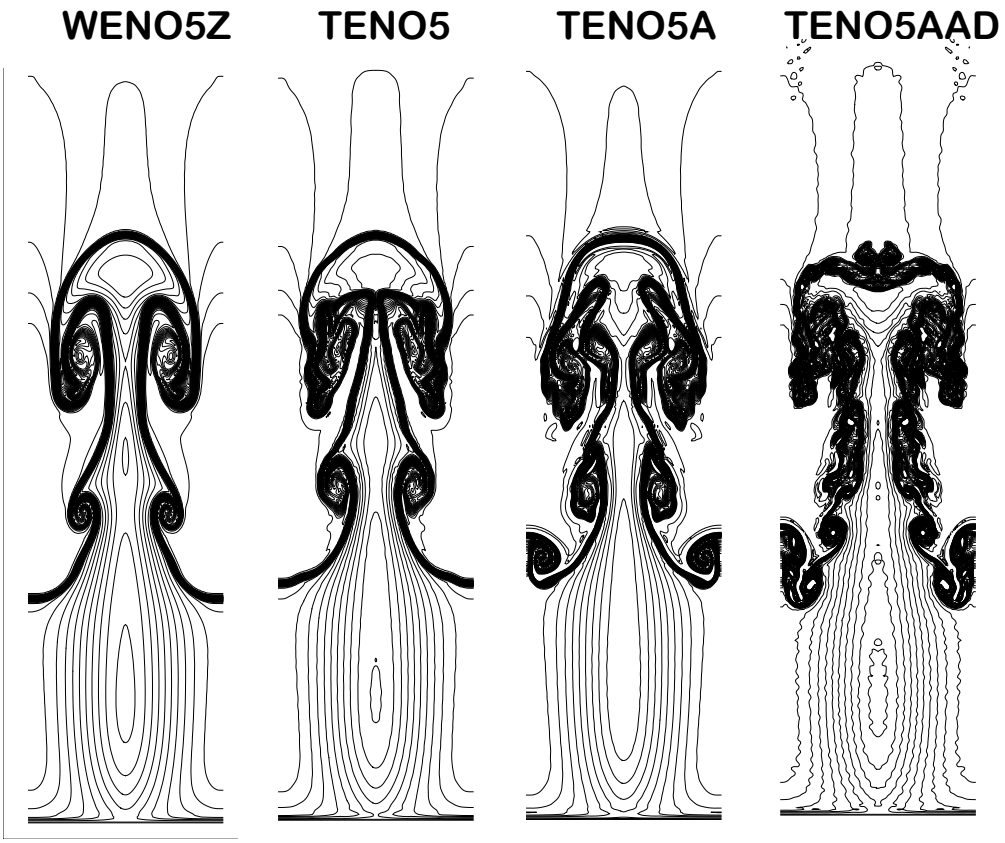

Figure 14: Rayleigh-Taylor instability: density distributions with 43 contour lines from 0.9 to 2.2. Mesh resolution is 128×512.

Table 5: Computational time per unit iteration of different schemes in milliseconds.

	WENO5Z	TENO5	TENO5A	TENO5AAD
128×512	84.93	99.75	109.288	111.684

4.7 2D shock-entropy wave interaction problem

We consider the two-dimensional shock entropy wave interaction problem proposed in [41]. The computational domain is $[-5,5]\times[-1,1]$ and the periodic boundary conditions are enforced in the y-direction. The grid resolution is 400×80 and the initial condition is given by

$$(\rho,u,v,p)=\begin{cases}(3.8571,2.6294,0,10.3333), & \text{if } x\leq-4,\\ (1+0.2sin(14xcos(\theta)+14ysin(\theta)),0,0,1), & \text{otherwise,}\end{cases} \tag{4.18}$$

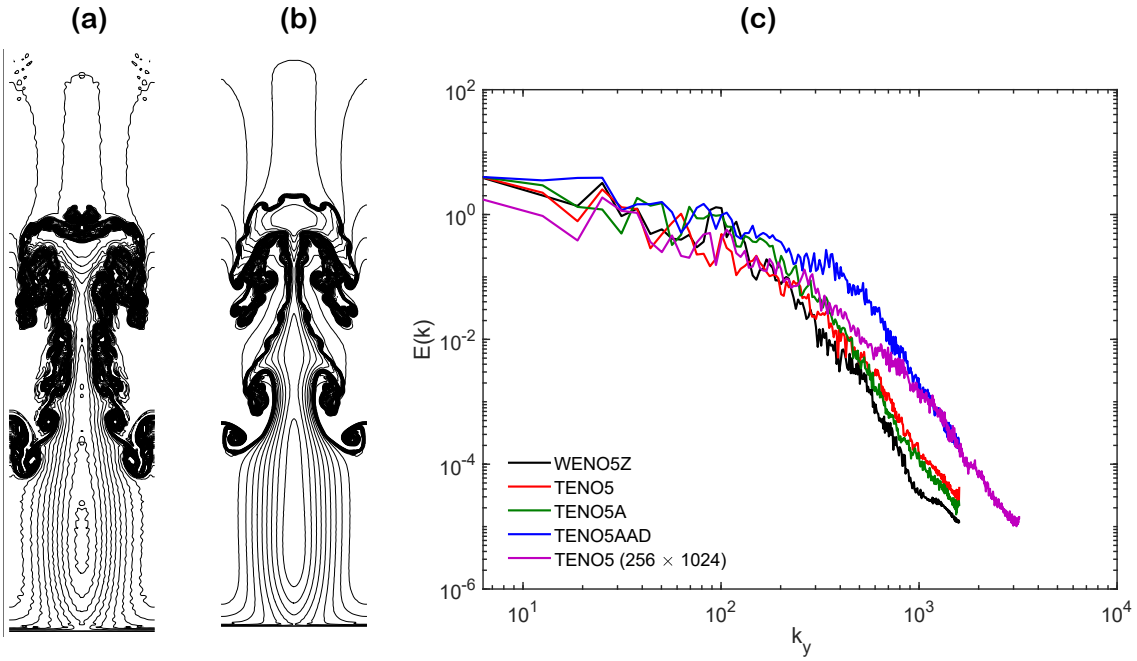

Figure 15: Density distributions: (a) TENO5AAD (128×512) and (b) TENO5 (256×1024). (c) y-direction energy spectra of WENO5Z, TENO5, TENO5A, TENO5AAD schemes with a resolution of 128×512 and TENO5 scheme with a resolution of 256×1024.

where $\theta=\pi/6$ denotes the angle of the initial sine wave relative to the x-axis. The initial solution is advanced till $t=1.8$. Fig. 16 presents the density contour at the final simulation time of different schemes. Compared with the other schemes, the TENO5AAD scheme can effectively capture shocks and resolve the high-wavenumber density field fluctuation with much higher resolution. This test case clearly reveals that employing artificial anti-diffusion attenuates numerical dissipation in the smooth region, whereas other techniques exhibit significant damping.

4.8 Double Mach reflection

The two-dimensional double Mach reflection from Woodward and Colella [39] is considered. The initial condition is

$$(\rho,u,v,p)=\begin{cases}(1.4,0,0,1), & \text{if } y<1.732(x-0.1667),\\ (8,7.145,-4.125,116.833), & \text{otherwise.}\end{cases} \tag{4.19}$$

The simulation is conducted within the computational domain of dimensions $[0,4]\times[0,1]$ till the time $t=0.2$. A Mach 10 shock is initially positioned at $x=1/6$ from the left boundary, inclined at an angle of 60° to the x-axis. Inflow and outflow boundary conditions are applied to the left and right boundaries. The lower boundary exhibits post-shock

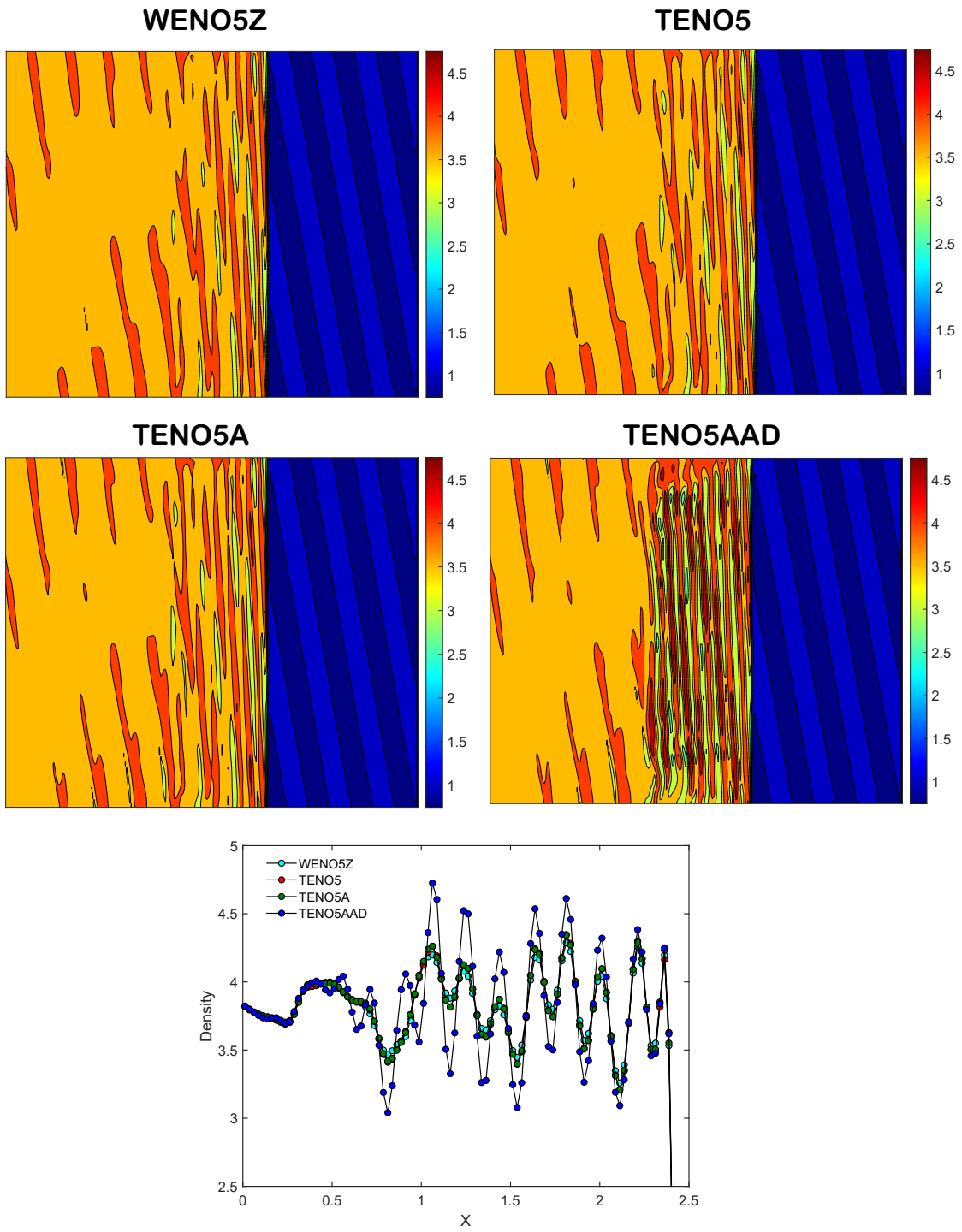

Figure 16: Shock-entropy wave interaction: density contours from 0.75 (blue) to 4.75 (red) in the region $[0,2.5]\times[-1,1]$. Bottom plot: Zoomed-in view of density distribution at the final simulation time along the x axis at $y=0$.

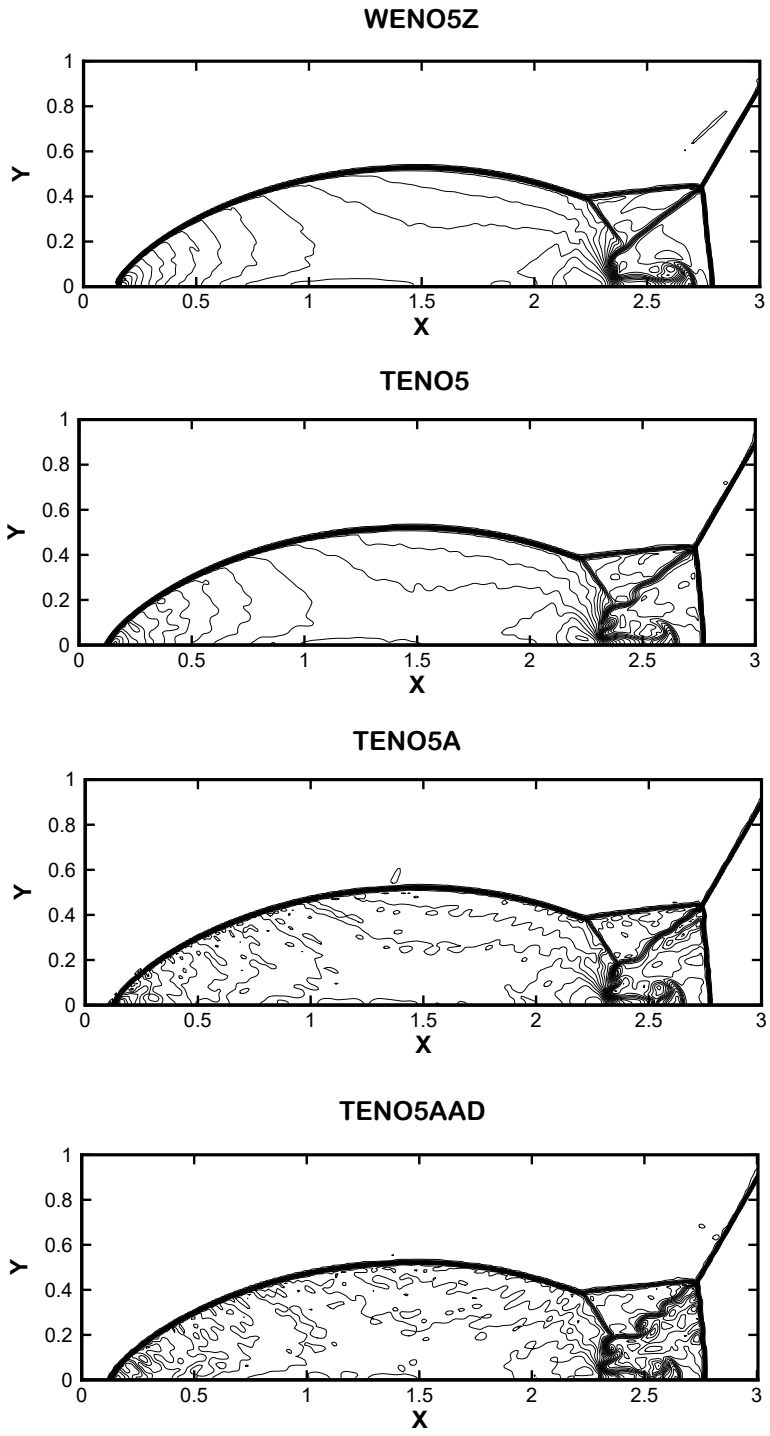

Figure 17: Double Mach reflection: density distributions with 43 contour lines from 1.887 to 20.9. The mesh interval is $\Delta x = \Delta y = 1/120$.

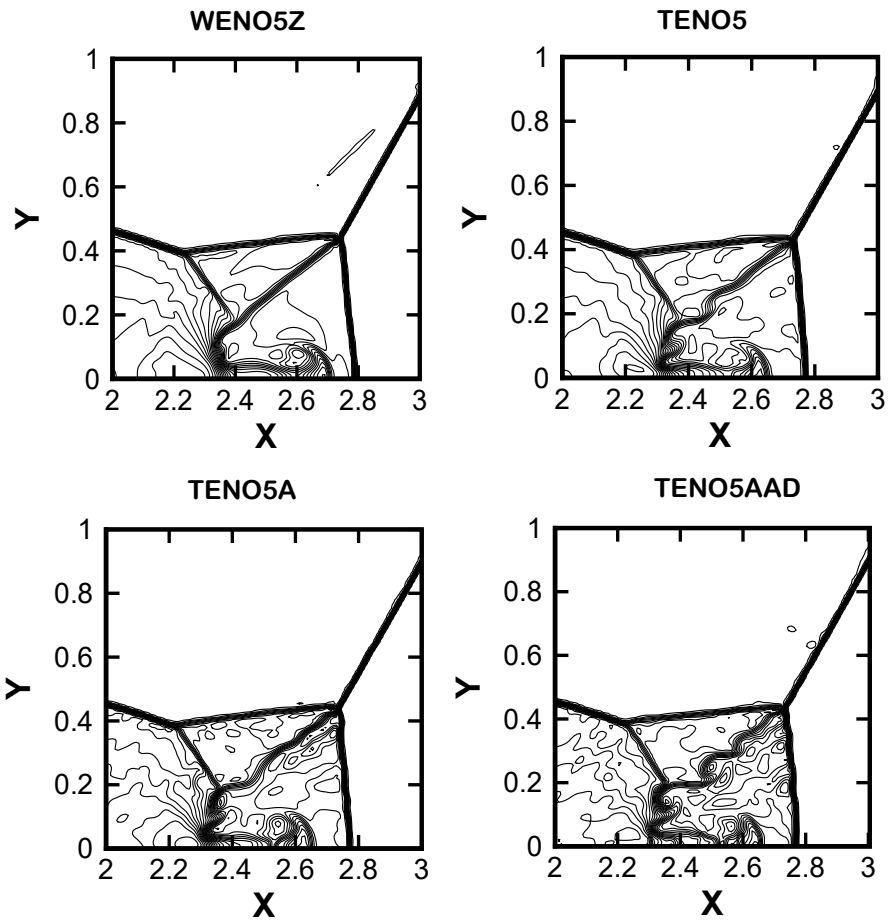

Figure 18: Double Mach reflection: density distributions near the Mach stems with 43 contour lines from 1.887 to 20.9. The mesh interval is $\Delta x = \Delta y = 1/120$.

conditions from $x = 0$ to $x = 1/6$, while a reflecting wall boundary condition is enforced from $x = 1/6$ to $x = 4$. The time-dependent boundary condition is applied to the upper boundary. To ensure numerical stability, the magnitude of $\widetilde{\alpha}$ is slightly relaxed as $1/75$, and the minimum value of Ω is set as -4. Figs. 17 and 18 illustrate the density distribution of WENO5Z, TENO5, TENO5A, and the current scheme with a mesh size of $\Delta x = \Delta y = 1/120$. The current TENO5AAD scheme has performed better in resolving Mach stems and exhibits greater resolution of fine-scale features.

4.9 2D shock and compressible mixing layer interaction problem

This test case is taken from [42] to assess the performance of the current scheme, which deals with the interaction of oblique shock with the spatially evolving compressible

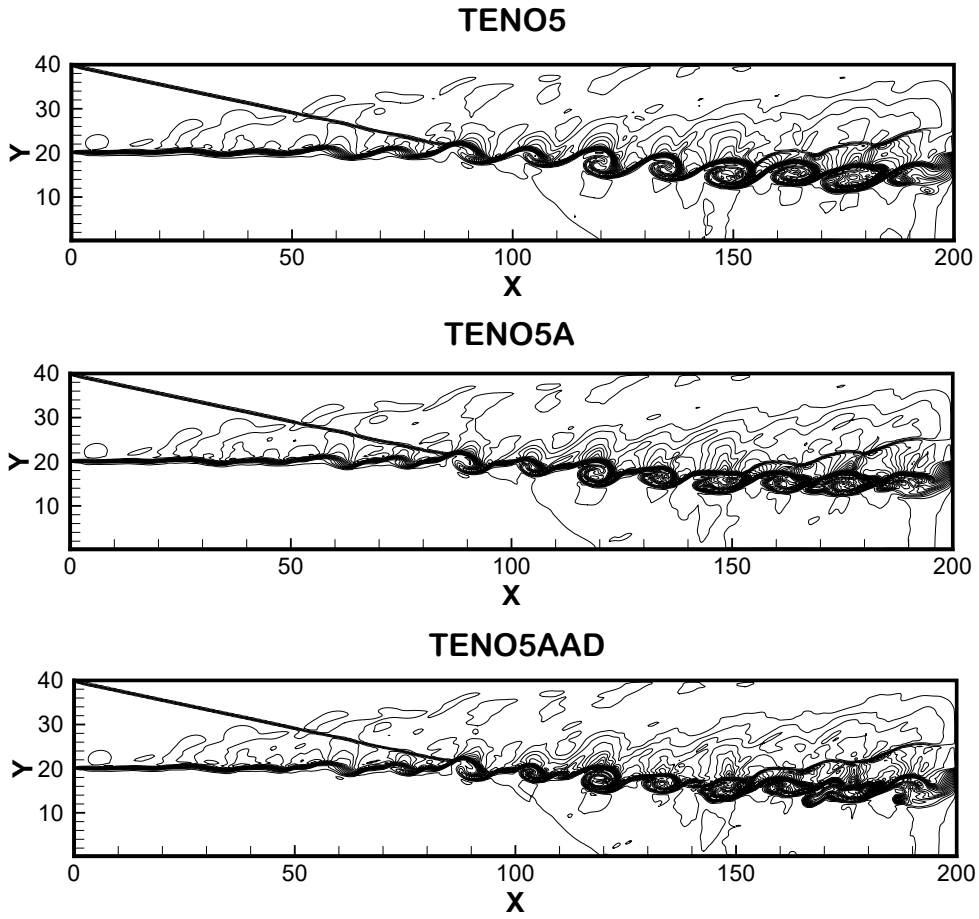

Figure 19: Shock-mixing layer interaction: density distributions with 30 contour lines from 0.3 to 3. Mesh resolution is 512×128.

mixing layer, resulting in a complex flow. The computational domain is chosen as $[1,200]\times[1,40]$. The inflow streamwise velocity is given by

$$u=\frac{1}{2}\Big[(u_1+u_2)+\tanh(2\hat{y})\Big] \quad \text{with} \quad \hat{y}=y-L_y/2, \tag{4.20}$$

where u_1 and u_2 are the freestream velocities. To trigger the roll-up and vortex pairing, the inflow fluctuations are added in the spanwise direction as

$$v'=\sum_{k=1}^{2}a_k\cos(2\pi kt/T+\phi_k)\,e^{(\hat{y}^2/b)}. \tag{4.21}$$

Here, $T=\lambda/u_c$ is the period, the wavelength $\lambda=30$. The constants are given by

$$(b,a_1,a_2,\phi_1,\phi_2)=(10,0.05,0.05,0,\pi/2), \tag{4.22}$$

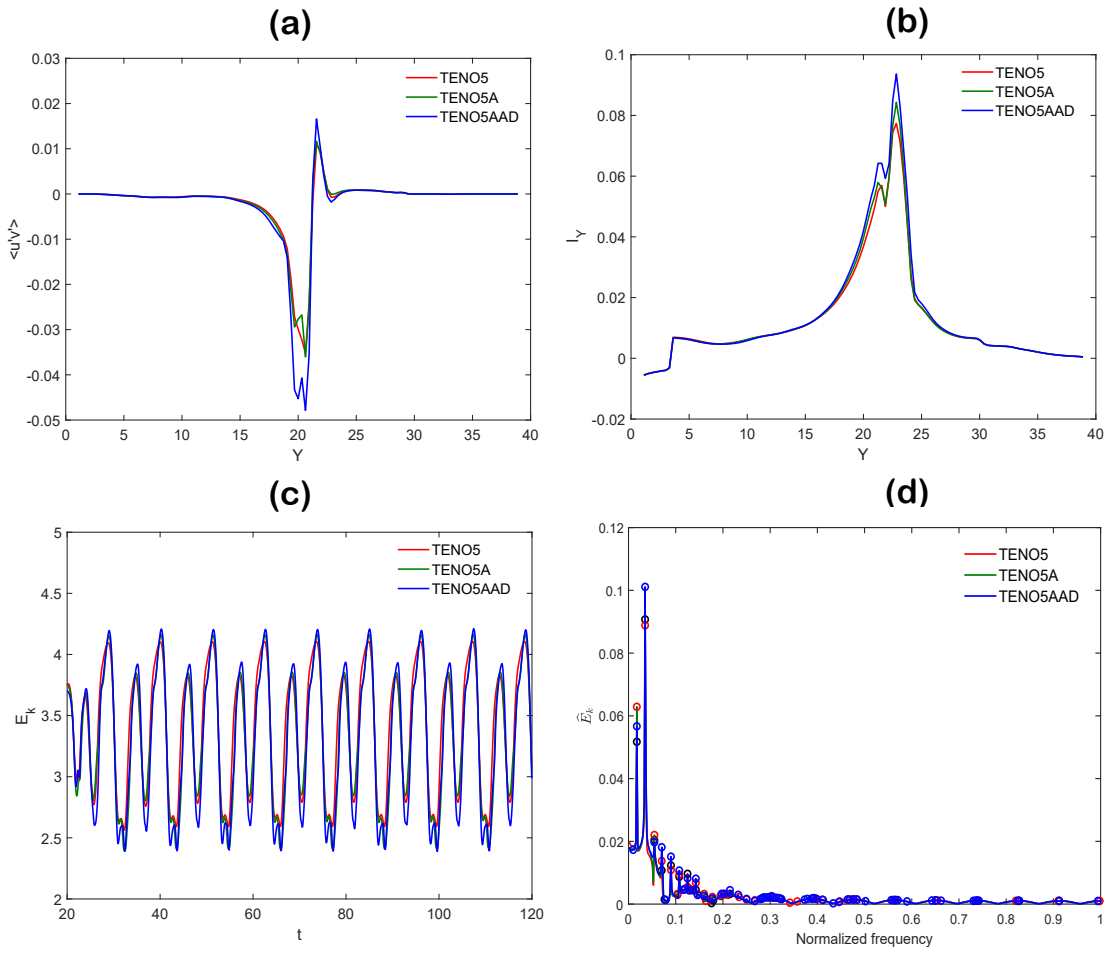

Figure 20: Shock-mixing layer interaction: at $x=150$ (a) Reynolds stress, (b) turbulence intensity, (c) time variation of total kinetic energy and (d) corresponding frequency spectrum.

and the flow parameters are

$$(\rho,u,v,p)=\begin{cases}(0.3626,2,0,0.3327), & \text{if } y<20,\\ (1.6374,3,0,0.3327), & \text{otherwise.}\end{cases} \tag{4.23}$$

The supersonic inflow and outflow boundary conditions are imposed on the left and right boundaries, while the reflecting boundary condition is assumed at the bottom boundary. The mesh resolution is 512×128 and the Reynolds number is $Re=500$. The density distributions at time $t=120$ of TENO5, TENO5A and TENO5AAD are shown in Fig. 19. It is noted that the proposed scheme captures more fine-scale structures. Fig. 20 presents the Reynolds stress and turbulence intensity at $x=150$ and the time evolution of the total kinetic energy and the corresponding frequency spectrum at this location. It reveals that

the new TENO5AAD scheme has much superior resolution characteristics compared to the standard TENO5 and TENO5A schemes.

4.10 Analysis of activation of anti-diffusive function

This section demonstrates the activation of the artificial anti-diffusive function for the one-dimensional numerical test cases presented earlier. The anti-diffusion is activated in the smooth region and near the discontinuities. Variables at the interface where λ_1 and λ_2 become zero are evaluated by the fourth-order central difference scheme. Figs. 21 and 22 show the final solution of the TENO5AAD scheme along with the values of λ_1, λ_2, and Ω for the one-dimensional Sod shock tube and shock-density wave interaction problems. It is evident that the anti-diffusion is not activated in the uniform regions, and both λ_1 and λ_2 are zero. Consequently, the flux is reconstructed using the fourth-order central difference scheme. The value of Ω is recorded as -8 in the smooth region, signifying reduced numerical diffusion. In the fluctuation regions where the function varies abruptly, the artificial anti-diffusion is enabled to attenuate the numerical dissipation for high-resolution. At the shock region, the standard TENO5 scheme with $C_T = 10^{-5}$ is applied in the reconstruction procedure. These observations coincide with Remarks 3.2-3.4.

5 Conclusion

In this study, a locally adaptive higher-order artificial anti-diffusion correction is used to manage the inherent numerical diffusion of the TENO5 scheme. The primary objective is to establish excellent resolution characteristics in the smooth region to resolve turbulent scales with minimal damping. The local switching parameter evaluates anti-dissipation, which is subsequently altered by introducing two free parameters. The values of the free parameters are fixed across all numerical simulations; however, these parameters can be changed depending on the complexity of the problem. The anti-diffusion term is altered locally about the switching function, ensuring a consistent reduction in numerical dissipation. The second coefficient in the reconstruction procedure eliminates the dissipation part of the polynomial while preserving the central part. This allows us to enforce the fourth-order central difference scheme in the flow's highly smooth region. These two techniques are paired with adaptive dissipation in the TENO5 scheme, which regulates the C_T value.

The findings of numerical experiments demonstrate that the proposed TENO5AAD scheme can capture more small-scale vortical features than previous schemes while maintaining a stable shock-resolving ability. This work can be improved by adjusting the free parameter based on local conditions to improve resolution. It can be used in various TENO schemes, including sixth-order (see A) and hybrid schemes.

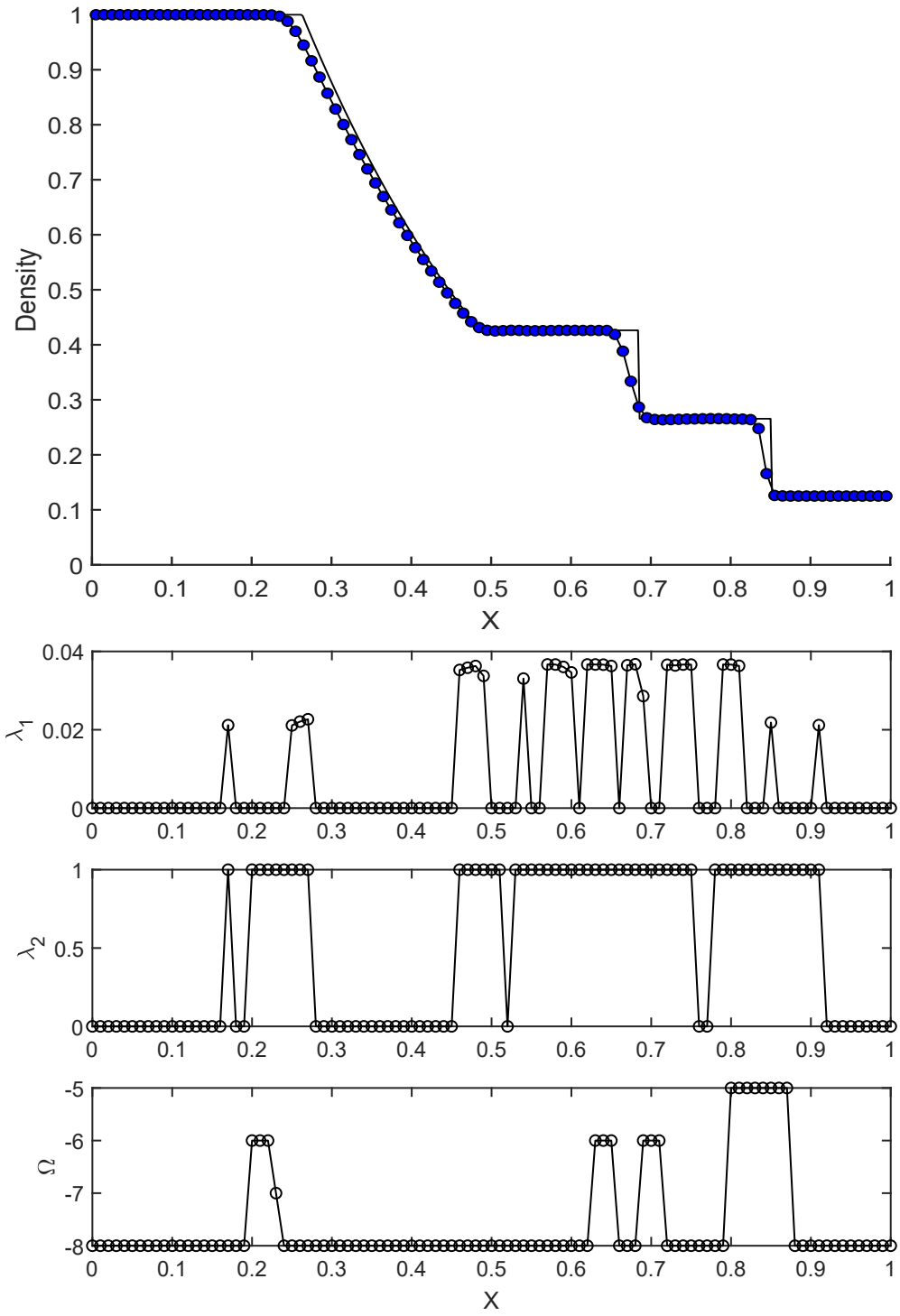

Figure 21: Sod shock tube problem: density distribution of TENO5AAD scheme (black line with symbols) at time $t=0.2$ with $N=100$ (top) and the magnitude of λ_1, λ_2 and Ω.

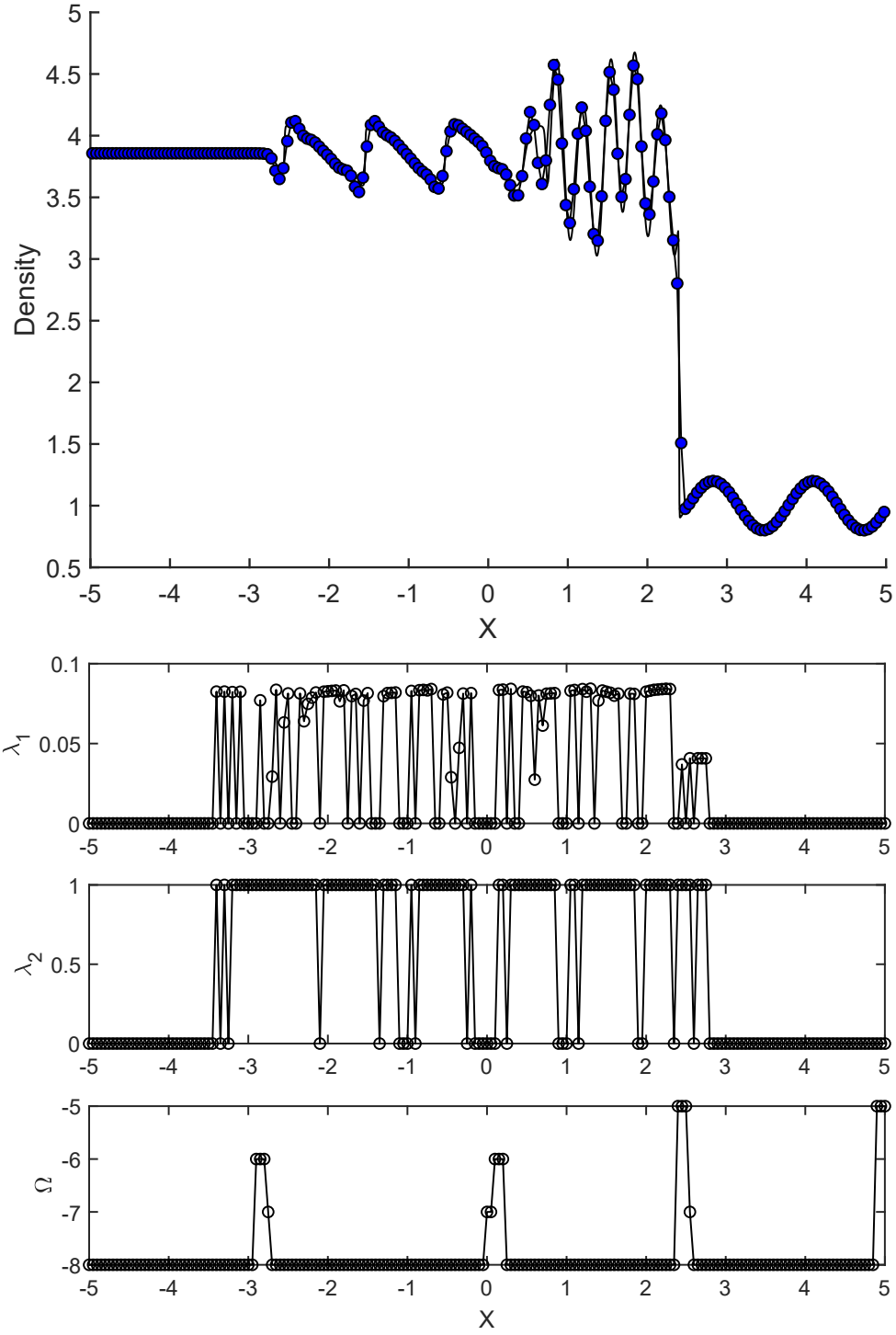

Figure 22: Shock-density wave interaction problem: density distribution of TENO5AAD scheme (black line with symbols) at time $t=1.8$ with $N=200$ (top) and the magnitude of λ_1, λ_2 and Ω.

Acknowledgments

We are grateful to the Indian Institute of Space Science and Technology for offering facilities and resources for this project. The High-Performance Computing (HPC) facilities and infrastructure provided by the institution facilitated the smooth execution of the research. This research work was supported by the Advanced Space Research Group [IIST/VSSC/03/2021/07].

A Sixth order TENO scheme with adaptive artificial anti-diffusion

It is obvious that the artificial anti-diffusive technique can be implemented in the sixth-order scheme with slight modification. The sixth-order TENO scheme developed by Fu et al. [19] is considered here. We integrate artificial anti-diffusion with variable C_T in the TENO6 scheme, and the numerical outcomes of one-dimensional Euler equation problems are presented.

For the TENO6 scheme, the flux at the interface can be split as

$$\begin{aligned}\hat{u}^+_{i+1/2} &= \frac{1}{12}\left(-u^+_{i-1}+7u^+_i+7u^+_{i+1}-u^+_{i+2}\right)\\ &\quad -\phi\left(\Delta u^+_{i-3/2},\Delta u^+_{i-1/2},\Delta u^+_{i+1/2},\Delta u^+_{i+3/2},\Delta u^+_{i+5/2}\right),\\ \hat{u}^-_{i+1/2} &= \frac{1}{12}\left(-u^-_{i-1}+7u^-_i+7u^-_{i+1}-u^-_{i+2}\right)\\ &\quad +\phi\left(\Delta u^-_{i+5/2},\Delta u^-_{i+3/2},\Delta u^-_{i+1/2},\Delta u^-_{i-1/2},\Delta u^-_{i-3/2}\right),\end{aligned} \tag{A.1}$$

where the dissipation function ϕ is defined as

$$\begin{aligned}&\phi(a,b,c,d,e)\\ &=\frac{1}{3}\omega_2(a-2b+c)+\frac{1}{6}\left(\omega_1-\frac{1}{2}\right)(b-2c+d)+\frac{1}{12}\omega_3(2b-5c+4d-e).\end{aligned} \tag{A.2}$$

The final reconstructed flux is expressed as

$$\begin{aligned}\hat{u}_{i+1/2} &= \frac{1}{12}\left(-u_{i-1}+7u_i+7u_{i+1}-u_{i+2}\right)\\ &\quad -\phi\left(\Delta u^+_{i-3/2},\Delta u^+_{i-1/2},\Delta u^+_{i+1/2},\Delta u^+_{i+3/2},\Delta u^+_{i+5/2}\right)\\ &\quad +\phi\left(\Delta u^-_{i+5/2},\Delta u^-_{i+3/2},\Delta u^-_{i+1/2},\Delta u^-_{i-1/2},\Delta u^-_{i-3/2}\right).\end{aligned} \tag{A.3}$$

The linear sixth-order approximation is given as

$$\hat{u}^C_{i+1/2}=\frac{1}{60}\left(u_{i-2}-8u_{i-1}+37u_i+37u_{i+1}-8u_{i+2}+u_{i+3}\right), \tag{A.4}$$

and the optimal weights are

$$\bar{\omega}_0 = \frac{9}{20}, \quad \bar{\omega}_1 = \frac{6}{20}, \quad \bar{\omega}_2 = \frac{1}{20}, \quad \bar{\omega}_3 = \frac{4}{20}. \tag{A.5}$$

The global smoothness is defined in undivided difference form as

$$\tau = \left| \beta_3 - \frac{1}{6}(4\beta_0 + \beta_1 + \beta_2) \right|. \tag{A.6}$$

The coefficient of the anti-diffusion term λ_1 is estimated to be analogous to that of the fifth-order scheme. The flux evaluated at the interface $x_{i+1/2}$ would be

$$\begin{aligned} \hat{u}^*_{i+1/2} = \frac{1}{12}(-u_{i-1} + 7u_i + 7u_{i+1} - u_{i+2}) \\ - \phi^* \left(\Delta u^+_{i-3/2}, \Delta u^+_{i-1/2}, \Delta u^+_{i+1/2}, \Delta u^+_{i+3/2}, \Delta u^+_{i+5/2}, \lambda^+_{1,i+1/2} \right) \\ + \phi^* \left(\Delta u^-_{i+5/2}, \Delta u^-_{i+3/2}, \Delta u^-_{i+1/2}, \Delta u^-_{i-1/2}, \Delta u^-_{i-3/2}, \lambda^-_{1,i+1/2} \right), \end{aligned} \tag{A.7}$$

where the modified dissipation function ϕ^* is defined as

$$\begin{aligned} &\phi^*(a,b,c,d,e,r) \\ &= \frac{1}{3}\omega_2(a-2b+c) + \frac{1}{6}\left(\omega_1 - \frac{1}{2} + 6r\right)(b-2c+d) + \frac{1}{12}\omega_3(2b-5c+4d-e). \end{aligned} \tag{A.8}$$

The $\lambda_{2,i+1/2}$ expressed in Eqs. (3.24) and (3.25) are deployed. However, here we impose the optimal (linear) weights in the smooth region rather than merely eliminating the dissipation term. Thus, the linear sixth-order central scheme in Eq. A.4 is adapted in the highly smooth region of the flow. Therefore, the nonlinear weights ω_k is given by

$$\omega_k = \begin{cases} \bar{\omega}_k, & \text{if } \lambda_{2,i+1/2} = 0, \\ \omega_k, & \text{otherwise.} \end{cases} \tag{A.9}$$

The density distributions of the numerical simulation of Sod shock tube, Lax shock tube, shock-density wave interaction and blast waves interaction problems are shown in Fig. 23. The proposed TENO6AAD scheme is compared with the standard WENO-CU6 [15] and TENO6 [19] schemes. It is noteworthy that the current scheme outperforms the existing schemes in all the test cases while resolving the discontinuity more sharply. Due to the limitations of this paper's length, we can only present one-dimensional solutions; however, this methodology may be readily adapted to two-dimensional test cases as described in Section 4. Nonetheless, we will defer this matter to future endeavours.

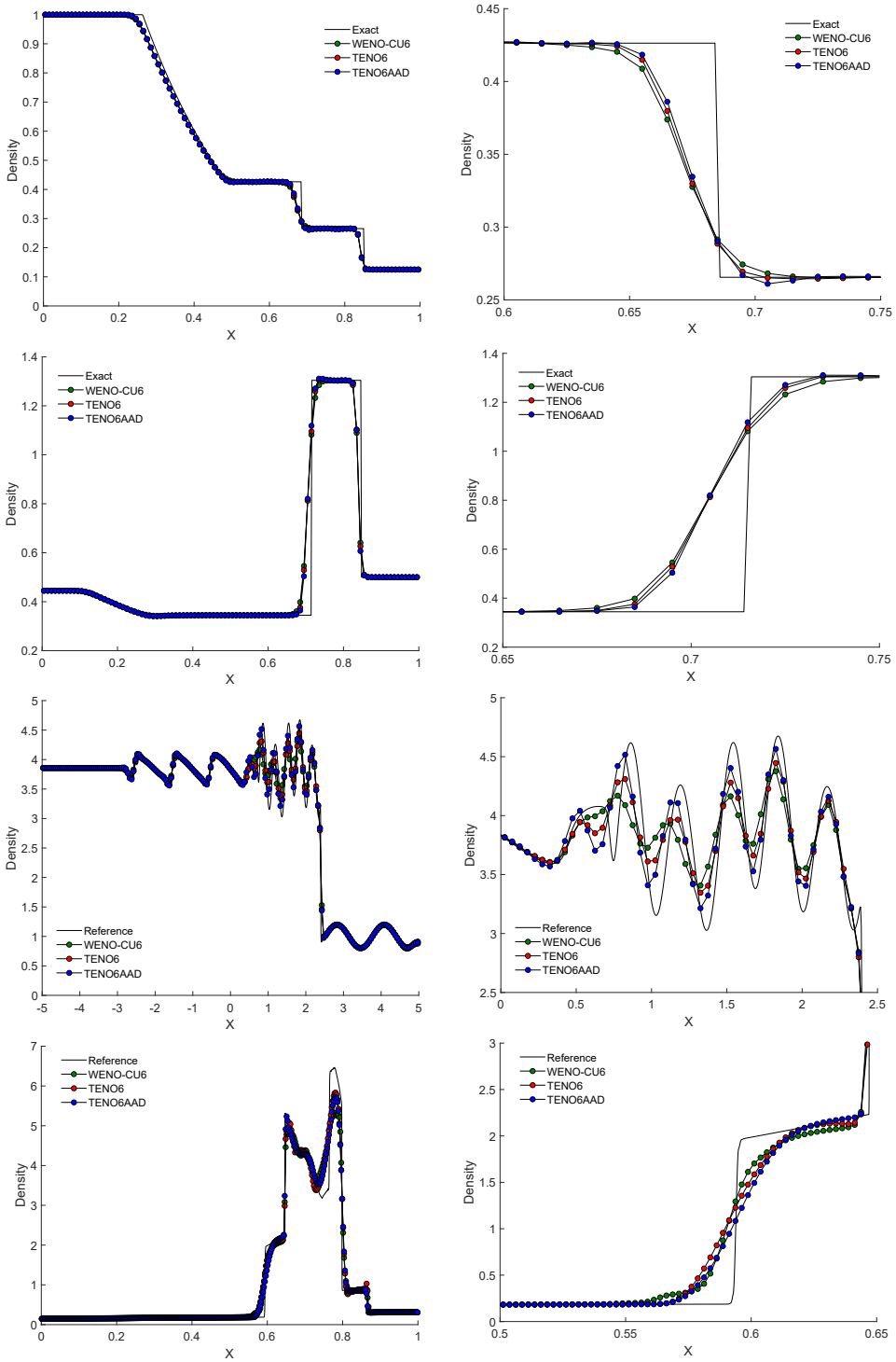

Figure 23: Density distributions of WENO-CU6, TENO6, and TENO6AAD schemes for one-dimensional problems (left) and the corresponding zoomed-in view (right).

References

[1] S. K. Godunov, I. Bohachevsky, Finite difference method for numerical computation of discontinuous solutions of the equations of fluid dynamics, Mat. Sb. 47 (89) (1959) 271–306.
[2] A. Harten, High resolution schemes for hyperbolic conservation laws, J. Comput. Phys. 49 (1983) 357–393.
[3] A. Harten, On a class of high resolution total-varaition-stable finite-difference scheme, SIAM J. Numer. Anal. 21 (1984) 1–23.
[4] R. K. Dubey, Flux limited schemes: Their classification and accuracy based on total variation stability regions, Appl Math Comput. 224 (2013) 325–336.
[5] D. Zhang, C. Jiang, D. Liang, L. Cheng, A review on TVD schemes and a refined flux-limiter for steady-state calculations, J. Comput. Phys. 302 (2015) 114–154.
[6] A. Harten, ENO schemes with subcell resolution, J. Comput. Phys. 83 (1) (1989) 148–184.
[7] C. W. Shu, Numerical experiments on the accuracy of ENO and modified ENO schemes, J. Sci. Comput. 5 (1990) 127–149.
[8] C. W. Shu, S. Osher, Efficient implementation of essentially non-oscillatory shock-capturing schemes, J. Comput. Phys. 77 (1988) 439–471.
[9] C. W. Shu, S. Oshers, Efficient implementation of essentially non-oscillatory shock-capturing schemes, II, J. Comput. Phys. 83 (1989) 32–78.
[10] D. S. Balsara, C. W. Shu, Monotonicity preserving weighted essentially non-oscillatory schemes with increasingly high order of accuracy, J. Comput. Phys. 160 (2000) 405–452.
[11] G. S. Jiang, C. W. Shu, Efficient implementation of weighted ENO schemes, J. Comput. Phys. 126 (1996) 202–228.
[12] G. S. Jiang, C. C. Wu, A high-order WENO finite difference scheme for the equations of ideal magnetohydrodynamics, J. Comput. Phys. 150 (1999) 561–594.
[13] A. K. Henrick, T. D. Aslam, J. M. Powers, Mapped weighted essentially non-oscillatory schemes: Achieving optimal order near critical points, J. Comput. Phys. 207 (2005) 542–567.
[14] R. Borges, M. Carmona, B. Costa, W. S. Don, An improved weighted essentially non-oscillatory scheme for hyperbolic conservation laws, J. Comput. Phys. 227 (2008) 3191–3211.
[15] X. Y. Hu, Q. Wang, N. A. Adams, An adaptive central-upwind weighted essentially non-oscillatory scheme, J. Comput. Phys. 229 (2010) 8952–8965.
[16] Y. Ha, C. H. Kim, Y. J. Lee, J. Yoon, An improved weighted essentially non-oscillatory scheme with a new smoothness indicator, J. Comput. Phys. 232 (2013) 68–86.
[17] C. H. Kim, Y. Ha, J. Yoon, Modified non-linear weights for fifth-order weighted essentially non-oscillatory schemes, J. Sci. Comput. 67 (2016) 299–323.
[18] Z. Xu, C. W. Shu, Anti-diffusive flux corrections for high order finite difference WENO schemes, J. Comput. Phys. 205 (2005) 458–485.
[19] L. Fu, X. Y. Hu, N. A. Adams, A family of high-order targeted ENO schemes for compressible-fluid simulations, J. Comput. Phys. 305 (2016) 333–359.
[20] L. Fu, X. Y. Hu, N. A. Adams, Targeted ENO schemes with tailored resolution property for hyperbolic conservation laws, J. Comput. Phys. 349 (2017) 97–121.
[21] L. Fu, X. Y. Hu, N. A. Adams, A new class of adaptive high-order targeted ENO schemes for hyperbolic conservation laws, J. Comput. Phys. 374 (2018) 724–751.
[22] X. Y. Hu, N. A. Adams, Scale separation for implicit large eddy simulation, J. Comput. Phys. 230 (2011) 7240–7249.
[23] L. Fu, X. Y. Hu, N. A. Adams, Improved five- and six-point targeted essentially nonoscillatory schemes with adaptive dissipation, AIAA J. 57 (2019) 1143–1158.

[24] I. Wibisono, Yanuar, E. A. Kosasih, Fifth-order Hermite targeted essentially non-oscillatory schemes for hyperbolic conservation laws, J. Sci. Comput. 87 (2021) 1–23.
[25] L. Fu, Review of the high-order TENO schemes for compressible gas dynamics and turbulence, Arch. Comput. Methods Eng. 30 (2023) 2493–2526.
[26] S. Takagi, L. Fu, H. Wakimura, F. Xiao, A novel high-order low-dissipation TENO-THINC scheme for hyperbolic conservation laws, J. Comput. Phys. 452 (2022) 11089.
[27] T. Yang, G. Zhao, Q. Zhao, Novel TENO schemes with improved accuracy order based on perturbed polynomial reconstruction, J. Comput. Phys. 488 (2023) 112219.
[28] T. Liang, L. Fu, A new type of non-polynomial based TENO scheme for hyperbolic conservation laws, J. Comput. Phys. 497 (2024) 112618.
[29] Y. X. Ren, M. Liu, H. X. Zhang, A characteristic-wise hybrid compact-WENO scheme for solving hyperbolic conservation laws, J. Comput. Phys. 192 (2003) 365–386.
[30] Y. Li, C. Chen, Y. X. Ren, A class of high-order finite difference schemes with minimized dispersion and adaptive dissipation for solving compressible flows, J. Comput. Phys. 448 (2022) 110770.
[31] S. Pirozzoli, On the spectral properties of shock-capturing schemes, J. Comput. Phys. 219 (2006) 489–497.
[32] P. L. Roe, Approximate riemann solvers, parameter vectors, and difference schemes, J. Comput. Phys. 43 (1981) 357–372.
[33] V. V. Rusanov, The calculation of the interaction of non-stationary shock waves and obstacles, USSR Comput. Math. Math. Phys. 1 (1962) 304–320.
[34] S. Gottlieb, C. W. Shu, Total variation diminishing Runge-Kutta schemes, Math. Comput. 67 (1998) 913–915.
[35] N. Fleischmann, S. Adami, N. A. Adams, Numerical symmetry-preserving techniques for low-dissipation shock-capturing schemes, Comput. Fluids 189 (2019) 94–107.
[36] H. Wakimura, S. Takagi, F. Xiao, Symmetry-preserving enforcement of low-dissipation method based on boundary variation diminishing principle, Comput. Fluids. 233 (2022) 105227.
[37] G. A. Sod, A survey of several finite difference methods for systems of nonlinear hyperbolic conservation laws, J. Comput. Phys. 27 (1978) 1–31.
[38] P. D. Lax, Weak solutions of nonlinear hyperbolic-equations and their numerical computation, Commun. Pure Appl. Math. VII (1954) 159–193.
[39] P. Woodward, P. Colella, The numerical simulation of two-dimensional fluid flow with strong shocks, J. Comput. Phys. 54 (1984) 115–173.
[40] P. D. Lax, X. Liu, Solution of two-dimensional Riemann problems of gas dynamics by positive schemes, SIAM J. Sci. Comput 19 (1998) 319–340.
[41] F. Acker, R. B. Borges, B. Costa, An improved WENO-Z scheme, J. Comput. Phys. 313 (2016) 726–753.
[42] A. Chandhuri, A. Hadjadj, A. Chinnayya, S. Palerm, Numerical study of compressible mixing layers using high-order WENO schemes, J. sci. comput. 47 (2011) 170–197.